Earth and Space Science

Key Points:
- Color imaging and multispectral data allow remote unit definition and passive IR adds key remote mineralogical identification capability
- Most mineral phases present identified but discriminating amorphous phases, clay minerals, and oxides sometimes required dedicated procedures
- Fluorescence mapping and deep-UV Raman spectra detect organics in several sample locations, although organics spectral libraries need expansion

Supporting Information:
- Supporting Information S1

Correspondence to:
P. E. Martin,
pmmartin@caltech.edu

Studies of a Lacustrine-Volcanic Mars Analog Field Site With Mars-2020-Like Instruments

Peter E. Martin[1] [ID], Bethany L. Ehlmann[1,2] [ID], Nancy H. Thomas[1] [ID], Roger C. Wiens[3] [ID], Joseph J. R. Hollis[2], Luther W. Beegle[2], Rohit Bhartia[2], Samuel M. Clegg[3] [ID], and Diana L. Blaney[2] [ID]

[1]Division of Geological and Planetary Sciences, California Institute of Technology, Pasadena, CA, USA, [2]Jet Propulsion Laboratory, California Institute of Technology, Pasadena, CA, USA, [3]Los Alamos National Laboratory, Los Alamos, NM, USA

Abstract On the upcoming Mars-2020 rover two remote sensing instruments, Mastcam-Z and SuperCam, and two microscopic proximity science instruments, Scanning for Habitable Environments with Raman and Luminescence for Organics and Chemicals (SHERLOC) and Planetary Instrument for X-ray Lithochemistry (PIXL), will collect compositional (mineralogy, chemistry, and organics) data essential for paleoenvironmental reconstruction. The synergies between and limitations of these instruments were evaluated via study of a Mars analog field site in the Mojave desert, using instruments approximating the data that will be returned by Mars-2020. A ground truth data set was generated for comparison to validate the results. The site consists of a succession of clay-rich mudstones of lacustrine origin, interbedded tuffs, a carbonate-silica travertine deposit, and gypsiferous mudstone strata. The major geological units were mapped successfully using simulated Mars-2020 data. Simulated Mastcam-Z data identified unit boundaries and Fe-bearing weathering products. Simulated SuperCam passive shortwave infrared and green Raman data were essential in identifying major mineralogical composition and changes in lacustrine facies at distance; this was possible even with spectrally downsampled passive IR data. Laser-induced breakdown spectroscopy and simulated PIXL data discriminated and mapped major element chemistry. Simulated PIXL revealed millimeter-scale zones enriched in zirconium, of interest for age dating. Scanning for SHERLOC-like data mapped sulfate and carbonate at submillimeter scale; silicates were identified with increased laser pulses/spot or by averaging of hundreds of spectra. Fluorescence scans detected and mapped varied classes of organics in all samples, characterized further with follow-on spatially targeted deep-UV Raman spectra. Development of dedicated organics spectral libraries is needed to aid interpretation. Given these observations, the important units in the outcrop would be sampled and cached for sample return.

Plain Language Summary The Mars-2020 rover will land at Jezero Crater, where it will search for signs of past life and seek to refine our understanding of the geologic history of Mars. The ability to measure the minerals, chemical composition, and organic molecules present at the landing site is vital to these investigations. There are four instruments on the Mars-2020 rover which can make these measurements: SuperCam, Mastcam-Z, Scanning for Habitable Environments with Raman and Luminescence for Organics and Chemicals, and Planetary Instrument for X-ray Lithochemistry. We undertook a field study using instruments that approximate the same data that the Mars-2020 instruments will produce to discern (1) how the data from these instruments will inform and complement the discoveries from other instruments, (2) what limitations might exist for this suite of instruments and what important features may be missed because of these limitations, and (3) strategies to use the rover and its instruments most efficiently while lessening the gaps in knowledge that could result from these limitations. The data used to address these objectives compared favorably with a complete understanding of the field site using the full range of measurements available on Earth, indicating that accurate and complete information about the Mars landing site can be obtained while using the instruments in the modes described in this study.

1. Introduction

The Mars-2020 rover is an upcoming Mars Science Laboratory-class rover with a similar design to the current Curiosity rover operating on the surface of Mars. The 2020 rover will have a new instrument payload designed to address four main objectives: (a) explore and decipher the geological processes, history, and

past habitability of an astrobiologically relevant site on Mars; (b) search for potential biosignatures; (c) gather a cache of samples for return to Earth; and (d) prepare for human exploration of Mars (Mustard et al., 2013; Williford et al., 2018). Seven instruments were selected for the Mars-2020 mission to address these objectives: Mastcam-Z, a stereo multispectral imager; the Mars Environmental Dynamics Analyzer, a weather station; the Mars Oxygen ISRU Experiment, an in situ oxygen production experiment; the Planetary Instrument for X-ray Lithochemistry (PIXL), a microfocus X-ray fluorescence spectrometer; the Radar Imager for Mars' Subsurface Experiment, a ground-penetrating radar; the Scanning for Habitable Environments with Raman and Luminescence for Organics and Chemicals (SHERLOC), an autofocusing context imager and microfocus deep-UV Raman and fluorescence spectrometer; and SuperCam, a set of spectrometers capable of remote laser induced breakdown, Raman, and reflectance spectroscopies, along with a remote microimager. Four of these instruments (Mastcam-Z, SuperCam, SHERLOC, and PIXL) enable detailed imaging at multiple scales and spectroscopic measurements that provide information on mineralogy, chemistry, and organics at meter scale to micrometer scale. Such compositional data are essential to determining the geologic history of the landing site, assessing its paleohabitability, and searching for biosignatures. In addition to the measurements enabled by these instruments, the Mars-2020 rover will be capable of abrading potential targets to achieve a flat surface, removing dust from potential targets, and sampling targets by taking a core approximately 1 cm across and 5 cm long (Farley, 2017). The samples with the most potential for new discoveries will be cached for sample return, allowing thorough investigations to be conducted in laboratories on Earth.

As with other rovers, after landing, the Mars-2020 rover will explore regions of interest, the locations of which will be partially predetermined using orbital data. The general structure of a science campaign will begin with remote imaging from a distance of hundreds of meters, as the site of interest comes into view. This distant imaging will be followed up with imaging and spectroscopy of increasingly high resolution as the rover approaches the outcrop, allowing determination of some aspects of the composition of the units within a given outcrop and preliminary mapping of these units from a distance. Upon the rover's close approach to the outcrop, continued remote sensing will guide selection of targets for proximity science, that is, microscopic analyses using the instruments PIXL and SHERLOC. The full suite of contextual data collected by all of the instruments will then allow determination of the geologic and environmental history of the outcrop, which will guide the decision whether to sample a core from the near surface, and then which samples to add to the sample cache for possible return to Earth.

Each rover mission to Mars has so far carried a different instrument suite with distinct capabilities and modes of synergistic use as well as some limitations in measurement abilities. In this study, we examine how the Mars-2020 rover will detect composition (mineralogy, chemistry, and organics) and stratigraphic and petrographic relationships at a given outcrop to determine environmental history and habitability/habitation. Using an analog field site in the Mojave desert and a suite of field portable and laboratory instruments, we simulate the data that would be generated from the instruments most directly capable of measuring composition: Mastcam-Z multispectral, SuperCam, SHERLOC, and PIXL. A number of previous studies have undertaken similar Mars-like field studies using analog data (Arvidson et al., 2010; Johnson et al., 2001). The two remote instruments (Mastcam-Z and SuperCam) have heritage with instruments on the currently operating Curiosity rover (Malin et al., 2017; Maurice et al., 2012; Wiens et al., 2012), although both will have updated capabilities on Mars-2020. The other two instruments, SHERLOC and PIXL, will be used for proximity science; their microscale compositional mapping techniques have not yet been utilized in a planetary setting. The data sets produced by this instrument suite will therefore be novel in the context of Mars, and a full understanding of the synergies between and limitations of these instruments will be crucial to the success of the mission as a whole. Our study addresses stratigraphy at a local scale only insofar as is needed for environmental reconstructions by basic imaging. On Mars, Radar Imager for Mars' Subsurface Experiment may show radar reflections indicative of deep structural geology but such data are not collected here. We compare our Mars-2020-analog data and interpretations with the known composition and environmental history of the Mojave outcrop based on prior work (e.g., Hillhouse, 1987; Mason, 1948) and our field verification. This comparison allows us to reveal the synergies between the Mars-2020 instruments in terms of building an environmental history from an outcrop and discern which aspects of a given site can be easily determined and which aspects will be more difficult to address. Using these lessons, we suggest operating modes for the instruments, data collection, and

analysis protocols that maximize efficient use of the capabilities and limited resources available to the Mars-2020 rover, that is, time, power, and data volume.

2. Methods

The Mars-2020 instruments for compositional analysis and image-based contextualization were simulated using laboratory, field, and camera instruments (Table 1).

2.1. Imaging Simulation: Navcam and Mastcam-Z

Mars-2020's engineering reconnaissance capability consists of stereo navigation cameras (Navcam) on the mast, which provide 20 megapixel, three-color images at a resolution of 0.35 mrad/pixel with a 103° × 77° field of view (Maki et al., 2016). The science imaging instrument is Mastcam-Z, a mast-mounted, adjustable zoom, stereoscopic multispectral imager with heritage from the Mastcam instrument onboard the *Curiosity* rover (Bell et al., 2016), Pancam on the Mars Exploration Rovers (Bell et al., 2003), and the Imager for Mars on Pathfinder (Smith et al., 1997). It acquires RGB images with a multiple lens optical assembly and Bayer-patterned microfilters on a CCD detector over focus distances from 1–2 m to infinity at a resolution of up to 55–200 µrad/pixel (highest to lowest zoom; Bell et al., 2014). Images in 15 discrete visible/near-infrared (VNIR) channels from 440 to 1,013 nm are acquired using a filter wheel assembly (Bell et al., 2014; Buz et al., 2019). Mastcam-Z can characterize geomorphology, stratigraphy, and texture and is sensitive to variations in mineralogy, particularly for Fe-bearing minerals, which have distinctive absorptions in the VNIR wavelength range. It can also be used to aid in the operation, navigation, and target selection for the rover and other instruments.

Images collected using an iPhone 4s in standard photo mode were used to simulate basic color imaging capabilities of both Navcam and Mastcam-Z to provide context for the composition-focused study. A mosaic of these images was constructed using Adobe Photoshop CS 5.1 (Figure 1b). We do not simulate the stereo processing ability in this study. The resolution of the iPhone camera is 320 µrad/pixel (determined empirically using a photograph of a measuring tape; a formal assessment to determine Nyquist sampling was not performed). Thus, from distances of 35 and 2 m, respectively, the 11 mm/pixel and 64 µm/pixel resolution of the iPhone images acquired are similar to that of Mastcam-Z from 45 and 2.6 m and Navcam from 32 and 1.8 m.

The Ultra Compact Imaging Spectrometer (UCIS; Van Gorp et al., 2014) was used to collect a spectral image cube of the outcrop over wavelengths of 400–2,500 nm and a resolution of 1.4 mrad/pixel from a distance of 35 m. This spectral image was then subset and resampled to the Mastcam-Z detector and band-pass filters using the spectral resampling tool in ENVI to simulate Mastcam-Z multispectral imaging at an approximate distance of 193 m. These were used to create images of multispectral VNIR color variability of the outcrop, similar to what will be collected by Mastcam-Z. VNIR color differences were accentuated by using decorrelation stretches as is typical in analysis of Mars data (e.g., Farrand et al., 2006). Mastcam-Z spectra were simulated with data acquired by an ASD Fieldspec3 in the lab due to terrestrial atmospheric influences in the UCIS field data (e.g., a water vapor band at 940 nm) that will not be present on Mars. Representative individual bulk spectra of rock hand samples with a spot size of ~1 cm were acquired over the wavelength range 350–2,500 nm and subset and resampled to Mastcam-Z filter band passes.

2.2. SuperCam Simulation

SuperCam is a Mars-2020 mast instrument which will provide laser-induced breakdown spectroscopy (LIBS), remote pulsed green Raman spectroscopy (532 nm excitation), passive Visible (VIS; 400–850 nm) and Infrared (IR; 1,300–2,600 nm) spectroscopy, color remote microimaging (RMI), and a microphone to record sound (Wiens et al., 2017). This suite of capabilities allows SuperCam to detect mineralogy (VIS, IR, and Raman spectroscopy), chemistry (LIBS), and textures/morphology (RMI) without sample preparation. LIBS and Raman acquisition are active techniques, utilizing pulsed lasers, and can be acquired at distances up to 7 and 12 m, respectively, both at a spatial resolution of 0.7 mrad/spot. All other capabilities have no distance limitations other than atmospheric opacity. Passive VIS and passive IR have spatial resolutions of 0.7 and 1.15 mrad/spot and spectral resolutions of ≤12 and 30 cm^{-1}, respectively (Wiens et al., 2017). The RMI uses a Bayer-patterned CMOS detector to acquire color images with a field of view of 20 mrad and a resolution of 40 µrad/pixel (Gasnault et al., 2015; Wiens et al., 2017).

Table 1
Instrument Capabilities and Simulated Data Sets for Assessing Mars-2020 Instrument Performance

Instrument	Data to be generated	Simulated data	Data used
Navcam	RGB image 0.35 mrad/pixel 103° × 77° FOV	Color image at 135 m	False color UCIS image (R: 622, G: 552, B: 462)
Mastcam-Z	13 color image (including RGB) 55 μrad/pixel at best zoom 18° × 23° FOV at lowest zoom	Zoomed color image at 200 m Multispectral image at 190 m VNIR spectra	RGB iPhone image mosaic Spectrally downsampled UCIS image Spectrally downsampled ASD spectra
Supercam	0.7 mrad/spot 7 m distance limit	LIBS	LANL ChemCam-like instrument
	0.7 mrad/spot 12 m distance limit 532 nm excitation laser	Green Raman	Renishaw M-1000 microRaman spectrometer
	0.7 mrad/spot 10 cm^{-1} resolution 400–850 nm wavelength range	VIS passive	ASD spectra
	1.15 mrad/spot 30 cm^{-1} resolution 1300–2600 nm wavelength range	IR passive	Spectrally downsampled ASD spectra
	RBG image 40 μrad/pixel 20 mrad FOV	RMI	RGB iPhone images
	Sound	Microphone	Not simulated
PIXL	120 μm spot size 25 mm^2 scan area 28 kV X-ray energy	Micro-XRF	LA NHM Horiba XGT-7200 micro-XRF
SHERLOC	100 μm spot size 7 × 7 mm scan area	Deep-UV Raman	JPL breadboard instrument (MOBIUS)
	248.6 nm excitation laser	Deep-UV fluorescence	JPL breadboard instrument (MOBIUS)
WATSON	0.30 mrad/pixel	High-resolution color imaging	iPhone 4s camera photos

RMI images were simulated using iPhone images taken from a simulated distance of 24 m from the outcrop (a simulated distance of 192 m). Passive spectroscopy from SuperCam was simulated using UCIS image-derived field spectra resampled to the wavelength range, spectral, and spatial resolution of the SuperCam VIS and IR spectroscopies. As with simulation of Mastcam-Z data, ASD spectra were used for detailed spectral analysis to avoid complicating terrestrial atmospheric effects. The SuperCam VIS spectral sampling of <1 nm is smaller than either UCIS (10 nm) or the ASD (1 nm), although known passive spectral absorptions are generally broader than 10 nm (Clark et al., 1990), and so we do not anticipate missing spectral features due to this difference. The SuperCam IR passive range of 1,300–2,600 nm extends slightly beyond the maximum range of UCIS and the ASD spectrometer, meaning that carbonate minerals, which have absorption bands centered from 2,500 to 2,600 nm, would be better characterized by SuperCam than the simulation instruments.

SuperCam LIBS data were simulated by data collected using the ChemCam testbed instrument at the Los Alamos National Laboratory (Clegg et al., 2017), and data reduction was completed using a simple model in an open-source, multivariate data reduction program termed PySAT (Anderson et al., 2017). Green Raman was simulated using a green Raman instrument at Caltech, a Renishaw M-1000 microRaman spectrometer. This Raman spectrometer is not a remote instrument, and so offers significantly higher detail and sensitivity than will be present on Mars-2020. The green Raman spectra were resampled to the SuperCam resolution of 10 cm^{-1} (Wiens et al., 2017). The Raman used at Caltech has a spatial resolution of 3 μm and, therefore, is able to target individual grains in a way that the SuperCam Raman instrument will not with its minimum spot size of approximately 1.5 mm at the ~2 m mast height. Due to the active nature of Raman spectroscopy, downsampling the spatial resolution of the Renishaw M-1000 measurement is not possible. We do not anticipate significant spectral changes as a result of these differing resolutions, simply increased spatial resolution and decreased spatial footprint. A fluorescence background was subtracted from the green Raman data using a built-in cubic spline background removal tool in the WiRE program.
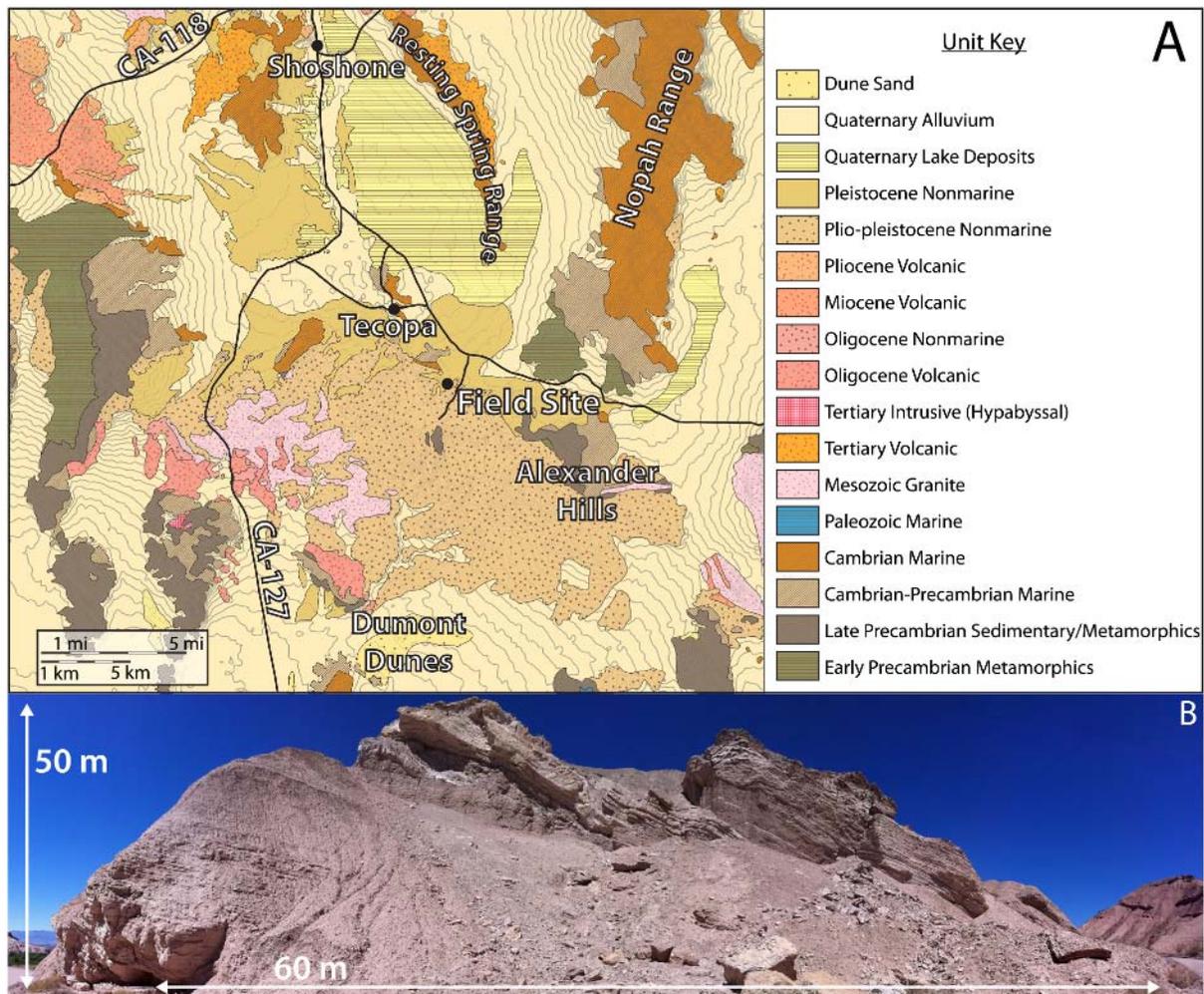
Figure 1. (a) A geologic map of the field site with 25-m contour intervals, modified from Jennings et al. (1962). (b) Photomosaic of the field site outcrop located at 35°48′25.5″N, 116°11′24.9″W.

2.3. SHERLOC Simulation

The SHERLOC instrument is an arm-mounted deep-UV fluorescence and preresonance/resonance Raman spectrometer, which is co-boresighted to a 10-μm/pixel greyscale autofocus and context imager (Beegle et al., 2015). Additionally, a built-to-print copy of the MArs Hand Lens Imager (MAHLI, 0.30 mrad/pixel; Edgett et al., 2009) has been added to the instrument (termed WATSON), allowing color imaging of samples (Beegle et al., 2017). A deep-UV laser with a spot size of 100 μm is scanned systematically across a 7×7 mm area to induce fluorescence, generating a compositional map of Raman and fluorescence spectroscopy, allowing the fine scale and bulk detection of organic compounds in a bulk material. This technique is typically able to detect $<10^{-6}$ weight fraction (w/w) concentrations of aromatics and $<10^{-4}$ w/w concentrations of aliphatics with a spatial resolution of 100 μm/pixel (Beegle et al., 2017). The deep-UV laser excitation wavelength of 248.6 nm was chosen to avoid mineral fluorescence, which occurs at wavelengths longer than 360 nm (Beegle et al., 2016). SHERLOC's capabilities allow characterization of the organic content and some mineral contents of a given sample, rastered and mapped spatially to reveal textures and patterns that can indicate the presence of potential biosignatures in the rock (Abbey et al., 2017).

SHERLOC-like spectra were acquired using a JPL prototype breadboard instrument named MOBIUS. Both instruments use pulsed 248.6 nm NeCu lasers (Photon Systems Inc.) as their excitation sources, but differ in their spectral resolution and optical focusing. With SHERLOC, deep-UV Raman and fluorescence spectra are collected simultaneously using a 1,200 lines/mm grating (resolution: 0.05 nm or 8 cm^{-1}), while

MOBIUS collects Raman and fluorescence spectra separately, using 1,800 and 300 lines/mm gratings, respectively (resolutions: 3.5 cm^{-1} and 0.16 nm). MOBIUS lacks the autofocus feature that provides SHERLOC a ± 8 mm tolerance to surface roughness (Beegle et al., 2017) and instead has a depth of focus of ± 500 µm. Therefore, the samples used in the laboratory were cut using an MK Diamond Products MK-100 Tile Saw to produce a flat face or carefully selected for a smooth surface. These sample preparation procedures will not be necessary during the Mars-2020 mission, although an abrasion tool is included on Mars-2020 for analysis of particularly weathered or rough surfaces. A commercially available DSLR camera was used to take context images of samples before measurement with MOBIUS, providing context images akin to those that will be acquired by WATSON of targets on Mars and used for interinstrumental comparisons. Other WATSON images (0.30 mrad/pixel) are replicated using an iPhone 4s (0.32 mrad/pixel) to image individual samples in a laboratory setting at high resolution.

2.4. PIXL Simulation

PIXL is an arm-mounted microfocus X-ray fluorescence spectrometer. PIXL directs a beam of 28 kV energy X-rays onto a sample and then examines a spectrum of intensity as a function of energy (Allwood et al., 2015). PIXL will be capable of rastering across a 25 mm^2 area at 120 µm/spot resolution to determine elemental abundance and distribution, correlated to visible textures in the rock imaged with a 50-µm/pixel micro-context camera with a field of view of 29×36 mm and illumination provided by an LED array (Allwood et al., 2015, 2016). The geometry of the PIXL instrument also allows rudimentary X-ray diffraction patterns to be collected; this capability is still under development (Schofield et al., 2017) and is not simulated in this study. The XRF measurements will allow determination of relative and absolute elemental abundances on small spatial scales, which will enable detection of past conditions that affect habitability and potential biosignature preservation.

Simulated PIXL data were acquired using a commercially available Horiba XGT-7200 micro-XRF at the Natural History Museum of Los Angeles, which was adjusted to acquire data at conditions similar to the specifications of PIXL (e.g., similar spot size, X-ray energy). Both instruments use a rhodium anode. While PIXL will have the ability to detect absolute abundances by applying a ground-based calibration for quantitative analysis of the measured spectra (Allwood et al., 2015), the data collected with the Horiba only provide relative abundances.

2.5. Field Site and Ground Truth Data Acquisition

A field site in the Tecopa Basin near the China Ranch oasis, located at 35°48′25.5″N, 116°11′24.9″W, was selected as the Mars-analog site (Figure 1). This locality is a Tertiary paleolake deposit (Hillhouse, 1987) with interbedded volcanic ashes and travertines. The mineralogy includes primary phases of quartz, feldspars, and pyroxenes, and secondary phases and chemical sediments that include phyllosilicates, sulfates, carbonates, chalcedony, and iron oxides. Several samples contained a significant percentage of less crystalline materials, which include smectite clays and/or X-ray amorphous components (Table 3). The strong 001 peaks and lack of a broad amorphous peak as observed in glasses and nanocrystalline alteration phases lead us to interpret that most of these materials are smectite clays. This mineralogical assemblage and especially the paleolacustrine environmental setting is relevant to anticipated geological observations at the Jezero landing site selected for Mars-2020 (Ehlmann et al., 2008; Fassett & Head, 2005; Goudge et al., 2015). The site was chosen over other nearby sites with basaltic lavas that are more directly mineralogically analogous because of the record of multiple environmental processes presented in multiple units with various mineralogies at a single outcrop. We discuss the implications of instrument suite capabilities for more basalt-rich lithologic units in section 4.2.1 (Table 2).

In order to compare the data and resulting geologic history generated from the simulated Mars-2020 instruments to the "true" geologic history of the field site, a ground truth data set was generated and used to construct a geologic history for this specific outcrop. The ground truth data set includes (1) background literature on the field site and the surrounding geology from prior researchers (e.g., Hillhouse, 1987; Jennings et al., 1962; Mason, 1948), (2) spectral analyses using the full resolution of UCIS, (3) field observations and geologic mapping (Figure 2, Table 2) combined with extensive sampling guided by UCIS spectral analyses, (4) high-resolution spectral analyses using spectra generated from an ASD Fieldspec3, and (5)

Table 2
Unit Names From Mapping Using Both Ground Truth Data (Figure 2) and Mars-Like Data (Figure 4)

Ground truth mapping unit name	Mars-like mapping unit name	Figures with additional Mars-like data
Qa (Quaternary alluvium)	SS (scree slope)	Figure 6
Lm1 (layered mudstone 1)	LB (layered brown)	
Lm2 (layered mudstone 1)	TL1 and TL2 (thick light)	Figure 5c
Mc (massive carbonate)	ML (massive light-toned)	Figures 5b, 6, 7, and 10
Lm3 (layered mudstone 1)	MD/LD (massive/layered dark)	Figures 5a, 6, 7, and 9
Lg (layered gypsum)	LL (layered light-toned)	Figures 5b, 6, and 7

Note. The first letter of each name refers to texture. Names from ground truth mapping use a lowercase second letter and refer to a geologic description, while the Mars-mapped units use an uppercase second letter and refer to the coloration of the unit.

X-ray diffraction patterns and derived mineralogy and flux fusion lithochemistry provided by Actlabs analytical services (Tables 3 and 4).

High-resolution ASD spectra were acquired using a contact probe with a built-in light source. White reference calibrations were performed after every five analyses. The assignments of spectral features in both the Mars-like data and ground truth data were made by comparison to spectral libraries and by direct expert analysis of specific spectral features in reference to the primary literature. The libraries used in this study include the RRUFF database for Raman spectroscopy and the JPL VNIR spectroscopy library (Grove, 1992). These libraries will be used during the Mars-2020 mission for the same purpose. Standard reference libraries for fluorescence spectroscopy are not available, as discussed below.

Based on the ground truth observations, the geologic history of the outcrop involves the deposition in a lacustrine environment of flat-lying clay-rich mudstones, which are finely laminated to massive and contain ~50 wt % smectite clays (mapped as units Lm1-3 in Figure 2). These mudstones are interspersed with felsic tuffs, which are weathered to have approximately 60 wt % smectite and 5 wt % zeolite. The smectite abundances described here are based on the abundance of smectite/amorphous reported in Table 3, the presence of a 001 peak, and the lack of an amorphous hump in the individual XRD patterns (available in the supporting information). These tuffs are of varying thicknesses and grain sizes, indicating different volcanic sources at different distances. The ash beds appear to have been deposited subaqueously in sequence with the mudstones. Bedding of larger grain size up to pebble conglomerates exist throughout the sequence and likely indicate major storm events. Extensive faulting has resulted in tilting, offset, and obscuration of the exact stratigraphic relationships between many of these strata, although a distal lacustrine environmental history appears to have been the dominant setting throughout deposition. A normal fault with a sense of motion into the plane of the page separates mudstone units Lm1 and Lm2. A massive travertine carbonate (unit Mc in Figure 2) with associated chalcedony exists as a lens within Lm2. The fenestral textures within the carbonate likely record microbial mat formation (Gandin & Capezzuoli, 2014). A large normal fault with an offset greater than the total exposed stratigraphic height within the outcrop has displaced upward the entire
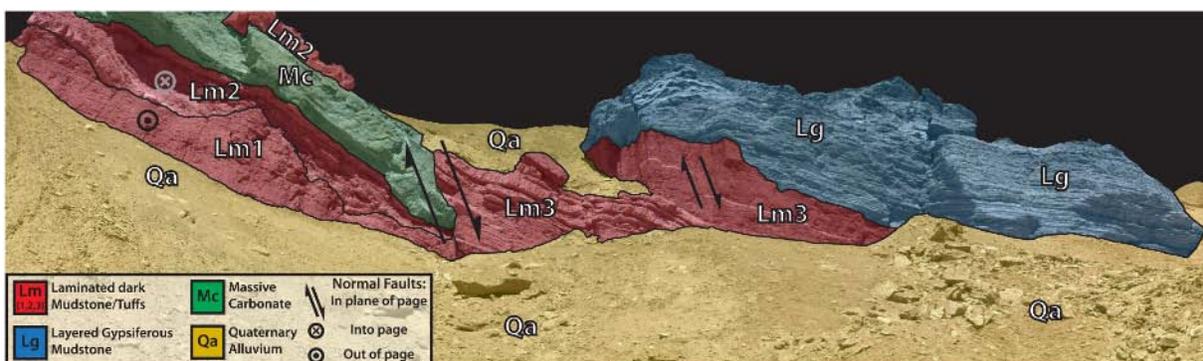
Figure 2. A unit map of the outcrop used in this study. See text for a detailed description of the geology of the site.

Table 3
Ground Truth XRD Results on Select Samples (All Measurements in wt %)

Sample number	CR002	CR003	CR008	CR012	CR018	CR019	CR025	CR026	CR028	CR029	TM	MB
Source unit (simulated Mars mapping)	MD/LD	Unmapped highlands	TL1	LL	LL	Unmapped highlands	ML	ML	SS	MD/LD	SS	
Source unit (ground truth mapping)	ML3 light layer	Lag deposit	ML2	GM	GM	Nearby highlands	MC	MC	Qa1	ML3	Loose cobbles	
Quartz	0.9	53.2	1.6	0.6	0.3	16.3	27		1.5	7.6	100	2
Tridymite							2.7					
Plagioclase	32.1	20.1	4.7			5.8			6.6	6.5		25
K-feldspar						3.9				17.4		3.2
Diopside												3.7
Orthopyroxene										3.9		
Muscovite		21.2	3.1			7.6			4.3	8.1		6.6
Chlorite		5.5				0.8						11.2
Amphibole												23.7
Clinozoisite												9.6
Clinoptilolite	2.6											
Calcite			63.7			43.5	57.8	100	67.8	13.2		
Dolomite						12.3						
Gypsum				87.2	86.4							
Anhydrite					6.5							
Celestine	2.8											
Smectite and amorphous	61.6		26.9	12.3	6.8	9.8	12.5		19.7	43.2		15.1
Total	100	100	100	100.1	100	100	100	100	99.9	99.9	100	100.1

Note. Relative accuracies are approximately ±3% (Hillier, 2016). Individual XRD patterns are available in the supporting information.

left-hand portion of the outcrop (units Lm1-2 and Mc) to a higher apparent stratigraphic height (i.e., the continuing strata cannot be traced in the outcrop; offset is perhaps hundreds of meters; Hillhouse, 1987). To the right of this fault mudstone/tuff laminae continue, mapped as Lm3. A disconformity exists at the top of the mudstone unit Lm3, above which interbedded mudstone and gypsum with fewer tuff beds was deposited (unit Lg in Figure 2), likely indicating a more saline lake environment with episodic drying. The mudstone strata within unit Lg either lack laminations or they exist at such a fine scale that the mudstone beds appear massive. Extensive dissolution and recrystallization has in many beds re-precipitated the gypsum into pure sparry selenite within unit Lg which exhibits little evidence of faulting.

Table 4
Ground Truth TOC and Lithochemistry Results on Select Samples (Measurements in wt %)

	CR002	CR003	CR008	CR012	CR018	CR019	CR025	CR026	CR028	CR029	TM	BM
TOC	0.59	0.56	0.83	0.70	1.63	1.46	0.92	3.53	0.65	0.74	0.54	0.55
TOC ±	0.15	0.15	0.19	0.16	0.10	0.12	0.13	0.33	0.16	0.15	0.15	0.14
SiO_2	52.5	74.2	16.6	6.2	2.6	30.7	43.5	1.0	16.8	47.5	96.1	48.2
Al_2O_3	16.7	11.1	4.3	1.7	0.6	4.7	0.3	0.2	3.7	12.6	1.0	14.9
FeO_T	4.02	4.32	1.88	0.83	0.22	1.65	1.01	0.09	2.29	4.54	2.14	14.00
MnO	0.07	0.07	0.22	0.02	0.01	0.03	0.03	0.00	0.46	0.13	0.01	0.21
MgO	3.21	1.29	1.33	0.56	0.31	2.83	0.35	0.51	2.21	2.55	0.08	5.58
CaO	3.86	0.79	39.87	29.10	31.84	30.42	29.94	54.51	37.86	9.49	0.19	8.58
Na_2O	2.69	1.92	0.56	0.13	0.07	0.58	0.06	0.03	0.38	1.31	0.02	2.66
K_2O	0.92	2.26	1.05	0.38	0.11	1.50	0.14	0.02	0.33	3.97	0.11	1.62
TiO_2	0.59	0.47	0.18	0.07	0.03	0.21	0.01	0.01	0.14	0.58	0.08	1.83
P_2O_5	0.19	0.11	0.09	0.03	0.03	0.08	0	0.04	0.05	0.23	0.03	0.24
C	0.03	0.12	8.08	0.19	0.02	7.03	6.48	11.40	8.08	1.82	0.03	0.03
S	0.48	0.01	0.04	16.10	18.20	0.03	0.03	0.09	0.04	0.29	0.04	0.04
Cl	0.04	0.02	0.06	0.02	0.01	0.02	0.01	0.04	0.10	0.06	0.01	0.07
LOI	14.5	2.1	32.8	25.4	20.9	26.8	24.7	43.0	34.1	15.5	0.6	2.7
Total	99.3	98.7	98.9	64.4	56.8	99.4	100.0	99.4	98.4	98.4	100.4	100.4

Note. Detection limits 0.01 wt % for all except MnO_2 and TiO_2, which have detection limits of 0.001 wt %.

3. Results of Mars-2020 Payload Simulation

3.1. Remote Sensing

3.1.1. Image-Based Remote Analysis

The simulated Navcam drive direction mosaic from a distance of 140 m (Figure 3) shows an outcrop composed of a number of intriguing units based on the textural and color differences present in the image. The mineralogical interpretations of the units in Figure 4a are described in section 3.1.2. All units dip toward the right of the image. A scree slope covers the lowest stratigraphic units and portions higher on the outcrop. The left-hand side of the outcrop has at least three units and the right-hand side has two stratigraphically higher units. The lowermost unit on the left-hand side is a layered brown (LB; all unit labels designated by Texture and Color) unit with layers a few centimeters in thickness. An apparent disconformity, possibly indicating subaerial erosion, separates this lower unit from a more thickly and irregularly bedded and folded light-toned (thickly bedded light, TL1) unit. A massive light-toned unit with color variation between white, yellow, and orange tones (massive light-toned unit, ML) lies above TL1. A second thickly bedded light unit (TL2) is stratigraphically at the top of the left side of the image. To the right of the image, there is a massive dark brown (massive dark, MD) unit containing a single thin, light-toned bed which runs parallel to the large-scale layering, suggesting that the MD unit may be laminated at a scale too fine to observe at the resolution of the simulated Navcam image (Figure 3). A unit with variable dark and light coloration (light-toned layered unit, LL) overlies the MD unit, with beds a few centimeters in thickness, slightly thicker than the beds in the LB unit. The LL unit exhibits alternating recessed bedding, possibly due to differential weathering, which could indicate that the unit has been exposed to weathering processes for a longer period than the other units. However, the recent scree below this unit is composed of larger blocks of a similar color, which may instead indicate that the LL unit is compositionally distinct from the lower units and contains more fissile material.

Based on the information available in the Navcam image, a Mastcam-Z color drive direction mosaic and zoomed Mastcam-Z color image would most likely be acquired over the area covered by the Navcam image to allow selection of remote sensing targets for more detailed mineral and chemical compositional investigations and vet areas accessible for future in situ science. This study does not attempt to replicate traversability challenges for the Mars-2020 rover, so all desired targets and samples were considered "accessible" for the purposes of data collection (see section 4.3 for operational considerations). A Mastcam-Z multispectral image would also be acquired over a subset of the drive direction, and Mastcam-Z's zoom capability would be applied in areas where the textural and stratigraphic relationships in the image are not clearly visible in the unzoomed imaging (Figure 3). SuperCam would likely target all of the major units described above to determine composition using the passive techniques (i.e., VIS, IR, and RMI) from this long distance. Preliminary proximity science targets could also be selected using the Mastcam-Z drive direction.

A simulated Mastcam-Z multispectral image is shown in Figure 4b, which depicts a decorrelation stretch (DCS) of bands 676, 527, and 445 nm (RGB; Farrand et al., 2006). In this color combination, rocks with spectral features indicative of iron oxides appear red due to a strong absorption near 535 nm (Morris et al., 1985). Cyan colors indicate fewer iron oxides or those of different mineralogy, that is, the TL1 unit and the thin light bed in the MD unit. The spectral differences mapped through this DCS suggest compositional differences between the thickly and finely bedded units and the existence of discrete iron oxide-bearing zones of MD and LL (Figure 4b). The ML unit on the left near the top of the section is unique in this color combination and stands out as having no iron-oxide related features. The zoomed Mastcam-Z images (Figure 5c) indicate that the MD unit, which was apparently massive, actually has visible fine-scale lamination in the zoomed image at the subcentimeter scale, and should be re-termed the laminated dark (LD) unit.

3.1.2. Spectrum-Based Remote Analysis

Selected single spectra from outcrop units, resampled to Mastcam-Z multispectral resolution, shows variations in iron oxidation, mineralogy, and crystallinity (Figure 6). Fe oxides are present in multiple units, for example, LD mudstone laminae and the scree slope, based on absorptions near 535 nm (Morris et al., 1985). Other units (or portions of units) are notable for their lack of Fe oxides, for example, the bright bed in LD, select beds in LL, and most of ML. The LL unit spectra occasionally display a downturn in the last Mastcam-Z filter band, indicative of hydration (Rice et al., 2010). Outside of these specific spectra, differences generally involve subtle shifts in the 535 nm band position and are difficult to detect by eye, especially given the relative weakness of Fe-related absorptions in the scene. The DCS enhances these spectral
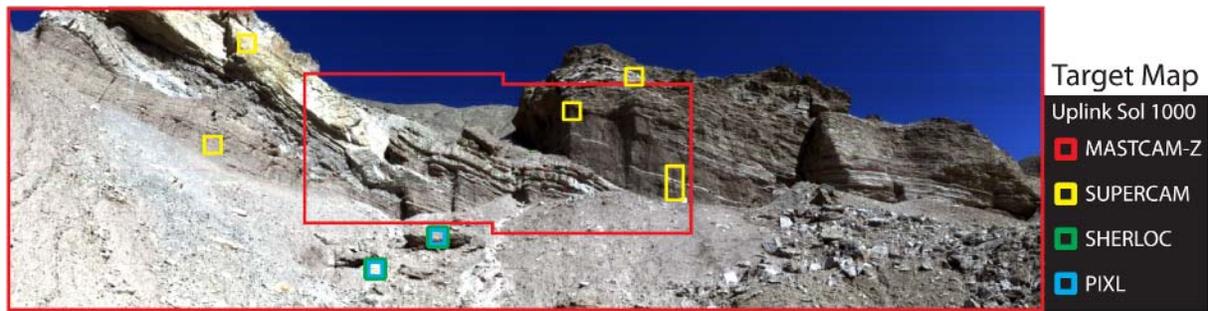
Figure 3. Simulated Navcam drive direction mosaic from a distance of 140 m. Examples of targets used in simulated remote sensing and proximity science are shown.

differences in a spatial context, allowing these slight differences to inform the delineation of putative units within the scene.

Passive IR spectra simulating SuperCam indicate the presence of phyllosilicates in each of the brown layered (LB), thickly bedded (TL1 and TL2), and layered dark (LD) units based on the presence of a metal–OH ~2,200 nm vibrational absorption (e.g., Figure 5a). The band center location of 2,210 nm is diagnostic of Al–OH, indicating the presence of montmorillonite (Clark et al., 1990). These units all have weak hematite-like 535 nm features in the VIS range (Morris et al., 1985), which are strongest in the LD unit. The ML unit has a strong 2,340 nm absorption and downturn toward 2,500 nm with no other diagnostic features (Figure 5b), suggesting that this unit is calcite-bearing (Hunt & Salisbury, 1971). The light-toned thin bed in the LD unit has similar spectral properties to the rest of the unit, although band depth trends indicate relative enhancement of montmorillonite compared to iron oxide (Figure 5a). The LL unit above the LD unit shows a mix of gypsum and montmorillonite spectral features (Figure 5b); lower in the unit, the montmorillonite-like spectral features dominate, which grades to progressively more gypsum-like spectra
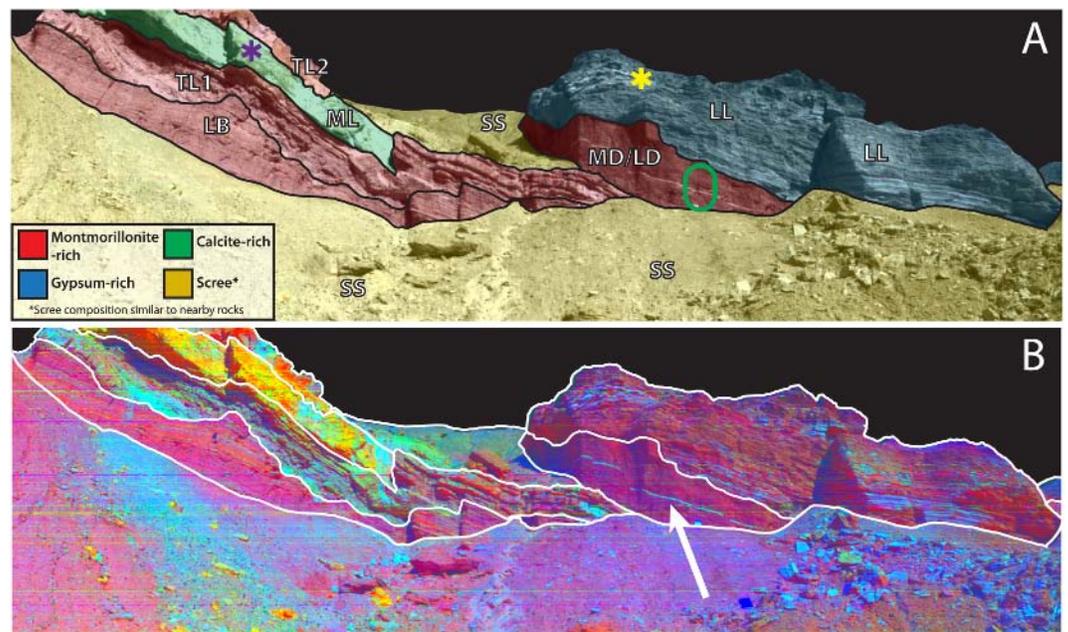
Figure 4. (a) A unit map derived from the remote sensing data acquired while approaching the outcrop (i.e., before proximity science and drilling). The inferred mineralogy is from the data shown in Figure 5. Unit abbreviations: LB = layered brown, TL1 and TL2 = thickly bedded light, ML = massive light, LD = laminated dark, LL = layered light-toned, SS = scree slope. Green oval, purple asterisk, and yellow asterisk denote the location of data shown in Figure 5. (b) Mastcam-Z-like DCS from UCIS data with bands at 676, 527, and 445 nm (RGB), showing variability in Fe-related phases in the outcrop. Unit outlines are delineated from a combination of color, texture, and DCS data as described in the text. A white arrow notes the location of a layer of ash (see section 4.1).
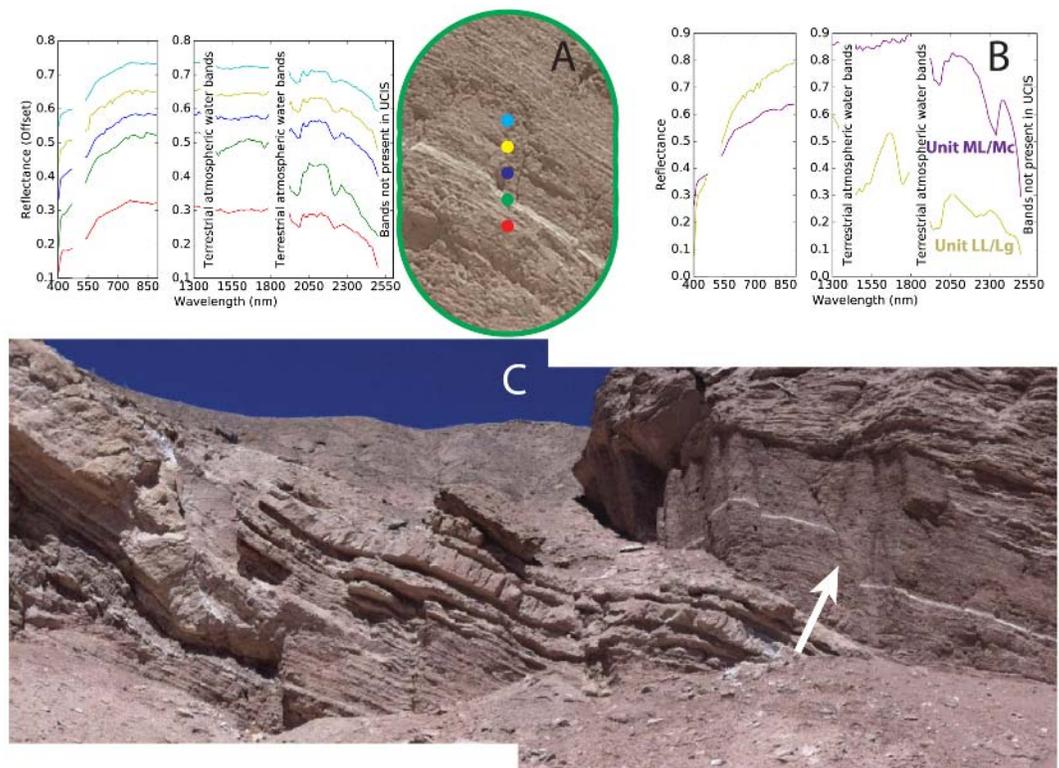
Figure 5. Select data from locations shown targeted in Figure 4. (a) SuperCam transect through unit MD/LD/Lm3, showing a discrete layer with an increased 2,200-nm Al–OH absorption from montmorillonite. While SuperCam does not cover much of the 530-nm region, the shallow spectral slope of the passive spectrum from this layer from 535 to 600 nm seen in the Mastcam-Z simulated data in Figure 4 suggests a decreased ~535-nm absorption from iron oxides. The simulated RMI resolution is approximately half that of the true RMI. The color of the spectra corresponds with the color of the circles in the RMI, which are accurate to the spot size of a SuperCam passive measurement. (b) Example reconnaissance spectra identifying the presence of carbonate (purple from unit ML/Mc; top left SuperCam target in Figure 4) and gypsum (yellow from unit LL/Lg; top right SuperCam target in Figure 4) in units ML and LL, respectively. SuperCam does not have spectral coverage 475–535 nm. This wavelength range is therefore not depicted in (a) or (b). (c) Mastcam-Z zoomed image of a fault (shown with white arrow) and laminations in unit MD/LD.

in the higher, lighter-toned units. Gypsum is detected by the diagnostic sharp triplet at 1,400 nm and absorptions at 1,700 and 2,200 nm (Hunt et al., 1971).

Upon arrival within a few meters of the outcrop, SuperCam's active techniques (Raman and LIBS) can be employed to further understand the mineralogy and determine the chemistry of the targets. Peaks in green Raman spectra confirm the presence of large amounts of calcite and gypsum in the ML and LL units (Figure 7). Montmorillonite was not detected in comparison with available spectral libraries; however, hydration-related features in literature spectra of clay minerals (Wang et al., 2015) are apparent. A montmorillonite standard analyzed on the same Raman instrument resulted in a good match to spectra from the clay-rich units (Figure 7i), indicating that clays are detectable with green Raman (at least with the in situ unit for this test), given adequate spectral libraries for comparison.

Principal component analysis of the reduced LIBS elemental chemistry data (Figure 8) clearly differentiates the gypsum and calcite samples from the silicates, while the silicates are distributed according to their major chemical constituents (e.g., limbs with increasing K_2O and Al_2O_3 suggest the presence of K-feldspar or micas). LIBS data show elemental compositions consistent with the evaporite minerals detected via VIS/IR and Raman spectroscopy: CaO present at ~30 wt % (gypsum, unit LL) and ~50 wt % (calcite, unit ML) level with no other major elements detected above ~5 wt % and major-element (oxides of Si, Ti, Al, Fe, Mg, Ca, Na, K) totals below 55 wt % (Figure 7). Gypsum and calcite can be distinguished by the presence or lack of relatively weak sulfur peaks at ~545, ~547, and ~563 nm to differentiate these two CaO-dominated
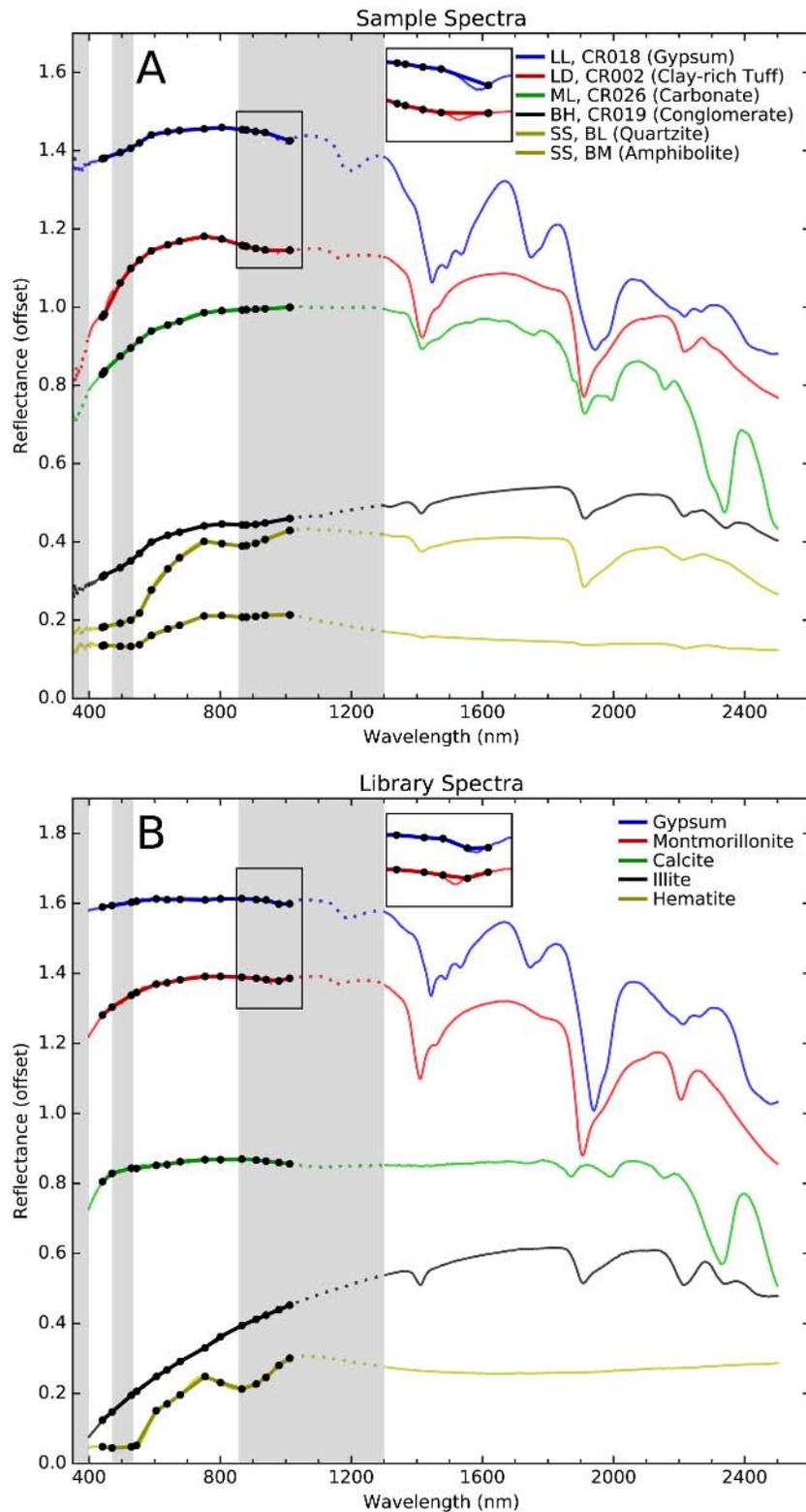
Figure 6. (a) Simulated Mars-2020 passive spectroscopy data acquired with an ASD spectrometer. Chemistry, mineralogy, and source units for all samples are given in Table 2. Mastcam-Z multispectral data are shown overplotted with black dots indicating filter locations. Light gray regions with dotted spectra indicate a lack of SuperCam passive coverage. The ASD spectra extend to 2,600 nm, while SuperCam passive IR will extend to 2,600 nm. Detail of the resolution of the hydration feature near 1,000 nm for gypsum- and montmorillonite-bearing rocks is shown in the blow-up box. (b) Library spectra corresponding to the mineral components in (a). Spectra are from the JPL spectral library (Grove et al., 1992).
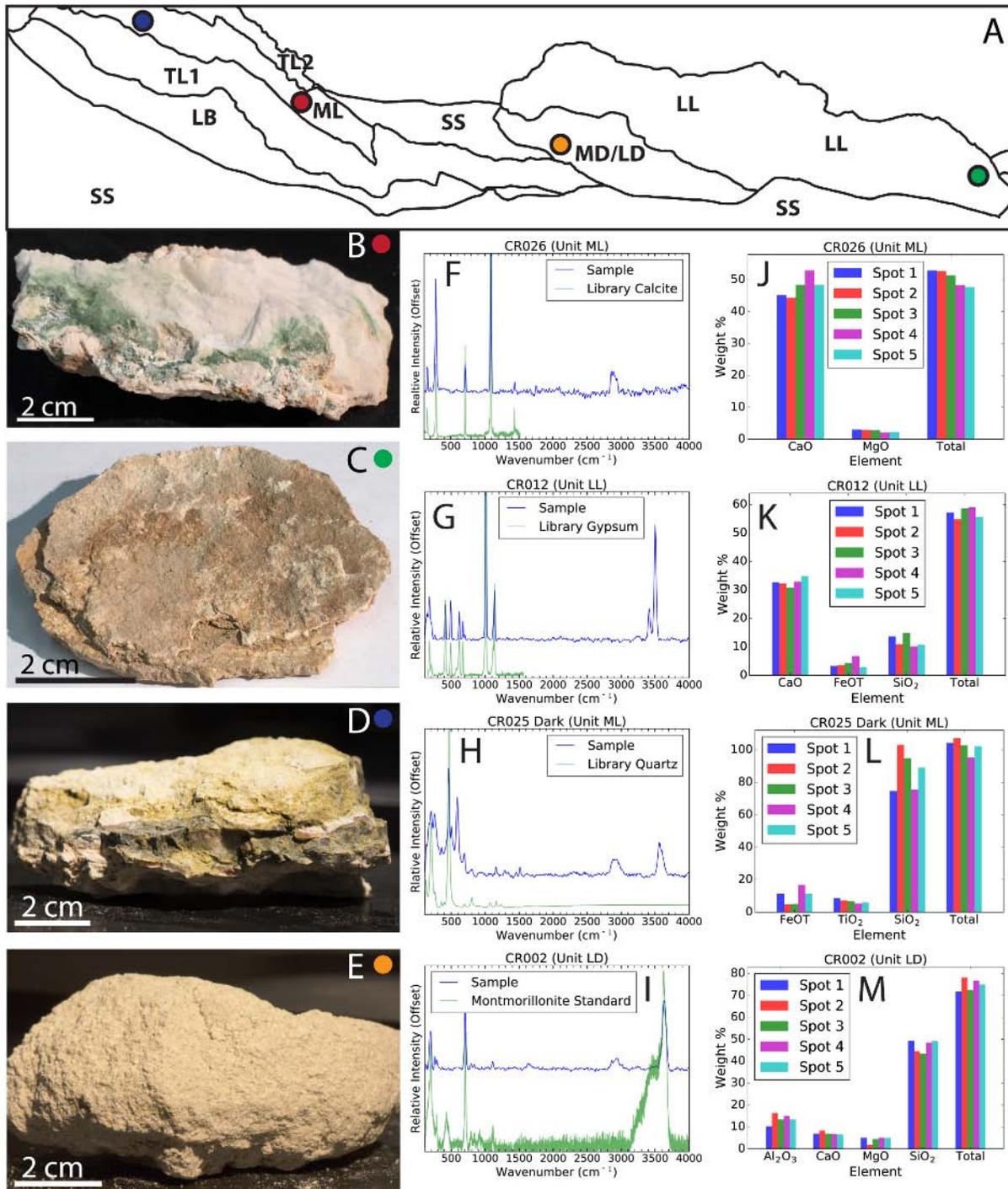
Figure 7. Close-approach data of the outcrop locations in (a) collected by simulated SuperCam, showing (b–e) RMI images for texture; images are representative and exact location of spectra are not shown (visible green areas in (b) are chlorophyll-bearing and were avoided in all analyses), (f–i) green Raman spectra for mineralogy, and (j–m) LIBS chemistry. Except for sample CR002, Raman library spectra (f–h) are taken from the RRUFF database and therefore extend only to 1,500 cm^{-1}. CR025 Dark (h) contains peaks that could not be matched with library spectra. Broad peaks near 3,500 cm^{-1} are related to OH/H_2O. LIBS oxide abundance data not shown are indistinguishable from 0 wt % within uncertainty; see Anderson et al. (2011) for a detailed discussion of LIBS uncertainties.

minerals (Figure 8). The gypsum sample (unit LL) has slightly higher than expected FeO_T and SiO_2, which are likely a result of clastic silicate and oxide minerals trapped in a primarily gypsum matrix, or could be a result of the relatively simple data reduction model used for LIBS in this study (discussed in section 4.2.2.
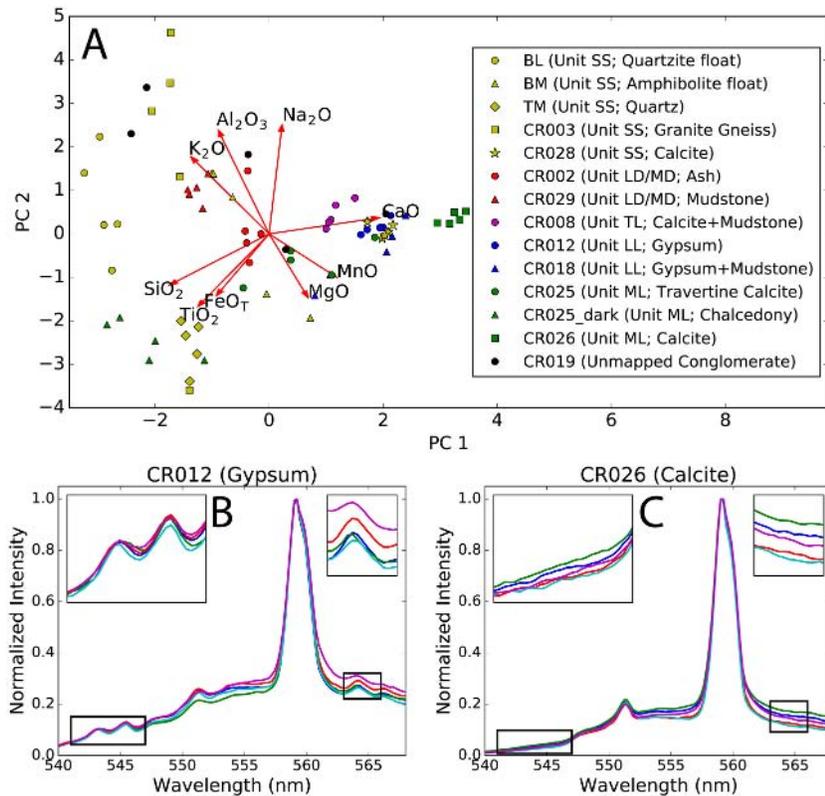
Figure 8. (a) Principal component analysis-based grouping of LIBS data. Individual LIBS spectra demonstrate the differentiation of (b) gypsum and (c) calcite using the small S peaks at 543, 545, and 563 nm. Calcite and gypsum are otherwise indistinguishable given just their bulk Ca-rich composition. The large peak at ~559 nm is calcium.

below). LIBS analysis of the clay-rich detrital sediments (sample CR002, unit LD) reveals aluminum-rich compositions with some additional potassium and calcium beyond what would be expected for pure montmorillonite, likely indicating the presence of minor gypsum, plagioclase and K-feldspars, illite, or muscovite (Table 5). The total elemental wt % measured in the typical mudstone is around 85%, potentially low due to the water of hydration present in the clay minerals or other volatile species, not quantified by this LIBS analysis. The loss on ignition for typical mudstone samples was ~15 wt % in ground truth lithochemistry analyses, well in line with this hypothesis (samples CR002 and CR029 in Table 4). Point-to-point variability within the rasters is low in individual beds of the mudstone LIBS data (generally within 5%, and almost always within 10%; Table 5 and Figures 7j–7m), indicating relatively homogenous composition.

Based on the remote sensing data presented above, a holistic picture of the geology of the outcrop with five major units begins to emerge (Figure 4a). Lowest in stratigraphic order are two distinct bedded montmorillonite-bearing units (LB and TL1) with minor iron oxide spectral features and bedding on the scale of a few centimeters (LB) and tens of centimeters (TL1), respectively. LB and TL1 are separated by a disconformity. The massive carbonate (ML) unit is potentially conformable with the TL1 and TL2 units, which are found both above and below. To the right of the scene, and not clearly related to the three units on the left, is a finely laminated unit composed of montmorillonite and iron oxide (LD), containing a light-toned bed having a stronger spectral detection of montmorillonite and a weaker iron oxide signature. Finally, an upper finely bedded (centimeter scale) unit of intermixed gypsum and montmorillonite (LL), with strong detections of gypsum in the upper beds tops the stratigraphic section, separated from LD by a disconformity. This disconformity between LD and LL appears to be an erosional contact based on the truncation of strata in the LD unit. Collectively, these units suggest a lacustrine environment with varying water chemistry which contains several unconformities indicating possible pauses in deposition. The float rocks, scree, and regolith at the base of the outcrop generally have the same spectral properties as the rock units

Table 5
Complete LIBS Results

Unit	Sample	Al$_2$O$_3$	CaO	FeOT	K$_2$O	MgO	MnO	Na$_2$O	SiO$_2$	TiO$_2$	Total
SS	BL	10.8	1.1	1.2	7.8	−0.5	−4.6	1.9	69.6	9.7	97.1
SS	BL	14.7	−0.8	2.3	8.8	0.4	−4.8	1.7	77.3	4.1	103.9
SS	BL	6.8	0.2	−0.8	5.8	0.7	−3.5	0.5	81.4	9.7	100.7
SS	BL	6.5	0.7	1.8	6.0	0.5	−4.3	0.6	76.9	9.8	98.6
SS	BL	7.7	1.7	21.3	3.2	0.5	−3.9	1.2	49.0	8.2	88.9
SS	BM	4.6	14.5	6.0	2.8	10.0	−5.5	−0.8	40.0	4.7	76.4
SS	BM	8.9	13.2	7.9	−0.4	9.9	−2.5	−0.5	35.6	4.8	77.0
SS	BM	17.9	6.5	5.3	2.7	3.7	−5.2	2.3	44.8	2.9	80.9
SS	BM	17.1	8.9	4.0	3.7	4.0	−5.3	1.4	44.9	2.7	81.2
SS	BM	16.7	8.3	6.1	1.7	4.4	−4.8	1.7	42.6	2.9	79.6
MD/LD	CR002	10.3	6.9	−1.4	0.5	5.0	−4.1	−1.2	49.4	6.3	71.8
MD/LD	CR002	16.3	8.4	3.5	1.2	1.8	−3.2	2.8	44.6	2.7	78.1
MD/LD	CR002	13.4	6.9	1.4	0.9	4.5	−2.8	0.3	43.4	4.6	72.5
MD/LD	CR002	15.1	6.8	0.2	1.3	5.1	−4.1	−0.6	48.5	4.4	76.7
BL	CR002	13.4	6.6	0.0	0.8	5.0	−4.1	−0.8	49.3	4.9	75.0
SS	CR003	28.9	1.7	5.0	5.2	1.4	−4.1	4.4	48.8	1.3	92.6
SS	CR003	22.8	3.6	3.6	7.7	1.8	−5.2	1.5	40.9	2.4	79.2
SS	CR003	33.9	2.7	2.6	5.6	1.0	−5.1	5.2	52.6	−0.9	97.6
SS	CR003	20.9	4.1	5.5	5.0	2.8	−2.4	1.9	35.6	6.5	79.9
SS	CR003	−3.2	−1.1	7.1	0.4	4.8	−1.0	−3.4	103.3	7.9	114.7
TL1	CR008	7.4	23.6	1.1	2.1	5.2	−3.0	0.1	32.9	1.3	71.0
TL1	CR008	5.6	29.5	0.8	2.4	4.4	−2.7	1.1	26.2	0.5	67.9
TL1	CR008	6.8	24.5	2.4	2.0	4.6	−2.7	0.5	29.1	2.1	69.3
TL1	CR008	7.2	26.5	1.5	2.4	4.5	−2.9	0.7	29.4	1.1	70.6
TL1	CR008	5.8	26.8	2.7	1.8	4.3	−2.9	0.3	26.8	2.9	68.3
LL	CR012	4.1	32.7	3.3	0.3	3.2	−2.5	0.3	13.6	2.2	57.2
LL	CR012	3.8	32.3	3.6	0.1	2.8	−1.3	0.7	10.9	1.9	54.8
LL	CR012	4.6	30.9	4.2	0.4	3.3	−2.2	0.2	14.9	2.3	58.7
LL	CR012	3.8	32.9	6.8	−0.5	2.5	−1.0	2.0	10.2	2.3	59.0
LL	CR012	3.1	34.8	2.9	0.7	2.9	−1.5	0.9	10.7	1.1	55.6
LL	CR018	1.9	39.5	0.4	0.1	1.9	−1.3	1.1	3.5	2.8	49.9
LL	CR018	2.5	16.6	9.5	2.3	5.2	3.5	2.5	21.0	8.4	71.4
LL	CR018	3.1	19.9	9.9	2.2	4.6	3.7	3.5	17.6	7.6	72.0
LL	CR018	3.7	31.3	−0.1	0.9	5.7	−1.8	−0.8	16.3	2.3	57.4
LL	CR018	2.5	32.8	5.5	0.4	2.8	2.1	3.4	6.5	4.9	60.8
SS	CR019	19.7	0.1	4.8	6.5	1.5	−4.3	6.9	66.3	2.8	104.4
SS	CR019	10.3	22.7	1.3	5.2	1.3	−5.5	0.3	27.2	2.2	65.0
SS	CR019	1.1	24.6	0.6	2.1	3.0	−4.6	−1.5	42.9	3.9	71.9
SS	CR019	17.5	2.3	5.8	6.2	0.8	−5.3	3.6	52.5	5.1	88.5
SS	CR019	1.0	40.0	−0.6	1.1	3.2	−3.8	0.1	10.3	1.9	53.3
ML	CR025	1.8	34.3	3.9	0.9	3.6	−1.5	0.5	19.4	1.9	64.8
ML	CR025	3.7	9.7	5.1	0.8	3.1	−3.3	−2.1	59.1	4.3	80.4
ML	CR025	6.0	18.7	4.4	2.0	4.2	−2.3	−0.6	42.0	3.1	77.5
ML	CR025	1.1	27.6	3.3	0.1	3.7	−1.9	−0.5	40.7	4.0	78.2
ML	CR025	5.7	19.4	5.3	0.9	4.3	−3.5	−0.8	40.8	3.1	75.1
ML	CR025_dark	0.1	2.3	11.3	2.6	5.1	1.2	−1.4	74.6	8.5	104.2
ML	CR025_dark	−2.3	−1.6	4.7	2.1	3.0	−3.6	−5.2	103.0	7.1	107.2
ML	CR025_dark	−1.2	−0.7	5.0	2.8	2.9	−3.3	−4.4	94.8	6.9	102.8
ML	CR025_dark	0.9	0.2	16.8	3.1	2.4	−5.9	−2.9	75.5	5.2	95.4
ML	CR025_dark	−0.2	−0.8	11.3	4.3	3.3	−6.4	−4.2	89.1	5.9	102.2
ML	CR026	−0.7	45.2	0.6	0.0	3.0	0.0	1.5	1.5	1.7	52.8
ML	CR026	−0.9	44.4	0.8	0.2	2.9	−0.4	1.7	1.8	2.4	52.7
ML	CR026	−1.5	48.4	−0.7	0.1	2.8	−0.3	1.3	−0.2	1.6	51.4
ML	CR026	−3.0	52.9	−1.7	0.3	2.1	−0.8	1.2	−4.3	1.8	48.3
ML	CR026	−1.8	48.4	−1.0	0.2	2.2	−1.0	0.9	−1.4	1.1	47.7
ML	CR028	2.0	35.9	−0.1	0.4	3.9	−3.3	−0.8	17.8	1.9	57.8
ML	CR028	2.6	36.1	−0.4	0.6	4.8	−3.3	−0.3	16.4	1.7	58.2
ML	CR028	2.1	36.0	−0.7	0.6	4.7	−3.4	−0.4	18.4	1.9	59.4
ML	CR028	3.5	33.4	−0.1	1.0	3.9	−3.4	−0.1	21.5	1.6	61.4
ML	CR028	2.6	36.6	−0.2	0.7	4.6	−3.2	0.0	15.9	1.2	58.2

Table 5
(continued)

Unit	Sample	Al$_2$O$_3$	CaO	FeOT	K$_2$O	MgO	MnO	Na$_2$O	SiO$_2$	TiO$_2$	Total
MD/LD	CR029	14.2	8.0	2.0	4.4	2.6	−4.7	0.9	49.5	3.0	79.9
MD/LD	CR029	13.9	5.4	1.7	4.5	3.2	−4.7	0.3	51.9	4.7	80.9
MD/LD	CR029	13.2	7.8	2.2	4.6	2.8	−4.7	0.7	49.0	4.4	79.9
MD/LD	CR029	13.7	6.1	1.6	4.6	3.1	−5.0	0.5	51.9	4.7	81.1
MD/LD	CR029	13.7	5.7	2.1	3.8	3.5	−4.1	0.2	51.1	4.8	80.7
SS	TM	3.0	1.1	16.6	−0.9	2.3	−3.2	−1.5	69.6	5.6	92.6
SS	TM	3.9	0.1	8.4	0.4	4.0	−2.1	−1.6	83.0	6.1	102.1
SS	TM	−4.4	−1.8	6.8	−0.6	4.4	−2.4	−2.6	102.5	7.8	109.7
SS	TM	0.3	1.5	9.5	0.3	2.8	−4.1	−1.7	85.6	5.5	99.6
SS	TM	−1.9	−0.4	7.9	−0.1	4.0	−2.6	−2.2	94.2	6.2	105.1

Note. Five raster points were taken on each sample.

above with a few outlier clasts, perhaps indicating longer distance transport. Based on this synthesis of information, the massive carbonate, sedimentary rocks with gypsum, and finely laminated, clay-bearing sedimentary units would likely be prioritized for proximity science.

3.2. Proximity Science

Proximity science data collection by SHERLOC/WATSON and PIXL typically would occur after the rover's arrival at select outcrop locations, guided by the remote sensing data described above. The reverse will also likely occur: unexpected findings from the proximity instruments will be followed up with further investigation using the remote sensing techniques in cases where those techniques (e.g., VIS/IR spectroscopy, LIBS, green Raman) may be informative.

WATSON-like microscopic imaging of units LB, LD, and LL indicates grain sizes smaller than the resolution of the imager (see color image of sample CR002 in Figure 9b), meaning that the individual grains are silt-sized or smaller. In combination with the fine lamination, this small grain size suggests a lacustrine origin, as was inferred by remote sensing data. The laminated fenestral texture of irregularly curled and wavy laminations in the carbonate indicates that it likely formed as a travertine deposit, possibly associated with microbial mats (see CR025 image in Figure 10a; as also interpreted by Gandin & Capezzuoli, 2014). The calcite is associated with a green and red solid, which forms botryoidal textures on the exterior of the rock (Figure 7d), and appears to alternate with the calcite in laminae. Green Raman demonstrates that this material is quartz (Figure 7h). LIBS observed relatively pure SiO$_2$ in these quartz veins with minor Fe and Ti (Figure 7l).

Simulated PIXL results demonstrate the ability to detect spatial patterns of major, minor, and trace chemistry. On a cut face of mudstone sample CR002 from unit LD (analogous to an abraded surface prepared by the Mars-2020 system), the spatial distribution of S, Si, and Ca reveals millimeter-scale laminae of gypsum and a new detection of calcium carbonate (not observed by the remote sensing instruments) within the phyllosilicate (Figures 9c–9e). The spatial distribution of Al and K suggests that Al-phyllosilicates and/or K-feldspar are present throughout the rock, and a band with Fe enrichment is also visible. Trace elements show coherent patterns, including spatially correlated Zr and Sr enrichments and laminae with Mn enrichment. Analysis of the carbonate sample CR025 from unit ML shows Ca with Si banding interpreted as laminae of quartz in a primarily calcite sample (Figure 10a). Based on WATSON-like imaging of texture, the quartz lacks visible structure and is likely a cryptocrystalline polymorph of quartz such as chalcedony. A lighter green lamination in this sample shows the presence of both Si and Fe, potentially indicating the presence of a secondary Fe-bearing phyllosilicate phase (Figure 10a). Samples that appeared spectrally to be pure gypsum (not shown) demonstrate the expected combination of Ca and S.

Fluorescence signals from organics were observed in all sample spectra ($n = 387$) and in three example low-resolution scan maps, utilizing 200-μm spacing and 25 laser pulses per point, replicating the quick scans likely to be done in an initial search for organics with Mars-2020 (Figures 9 and 10). The interior and
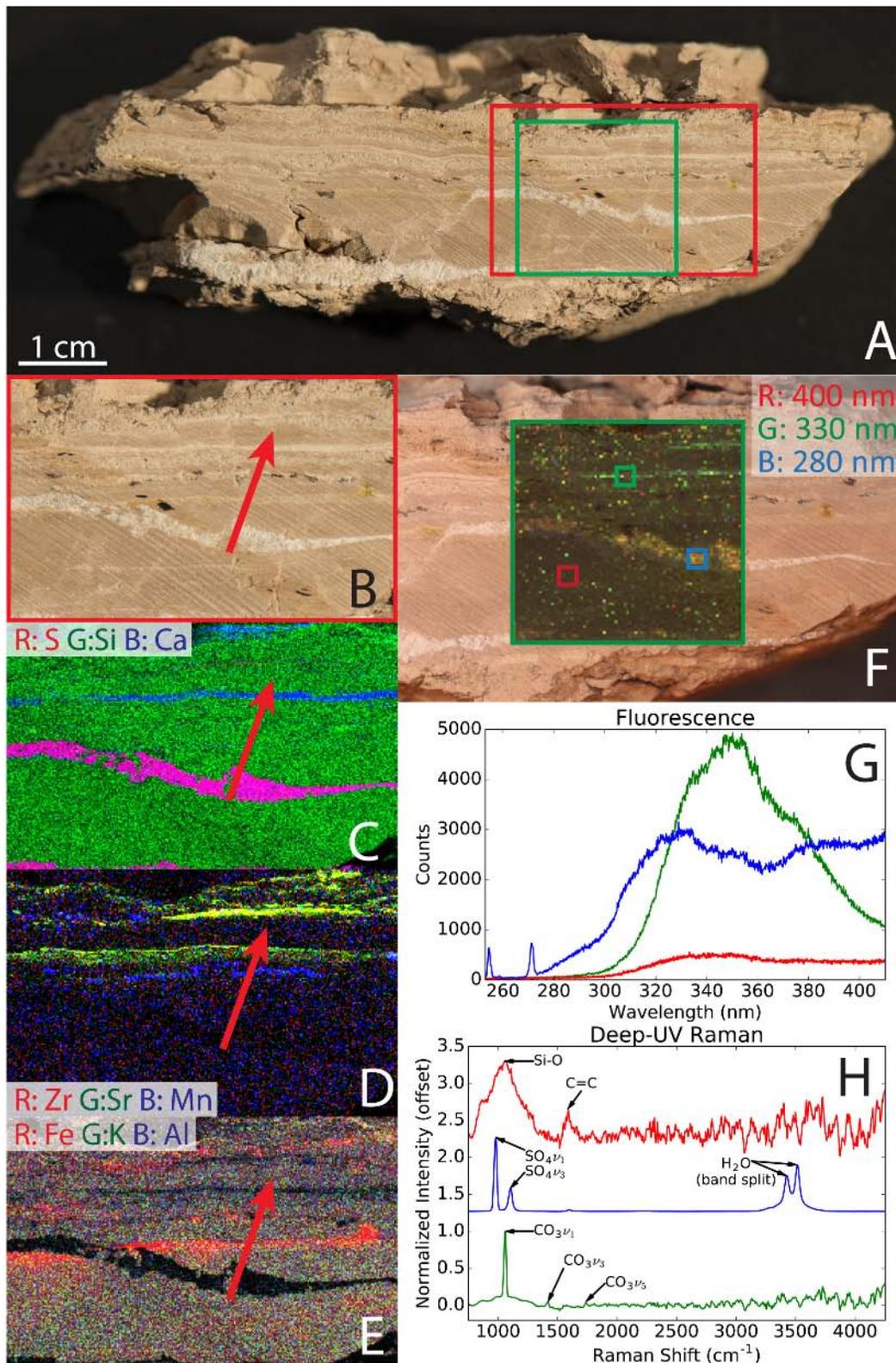
Figure 9. Proximity science results on phyllosilicate with gypsum and calcite bands (sample CR002, clay-rich unit LD). (a) Color image with the simulated PIXL area shown in red and the simulated SHERLOC area shown in green. (b–e) PIXL-like results for CR002. A red arrow notes the location of a spatially coherent band of Zr and Sr, which appears yellow in (d). (f) Low-resolution UV-fluorescence scan map, with (g) averaged fluorescence and (h) Raman spectra shown in the same color as the highlighted areas in (f).
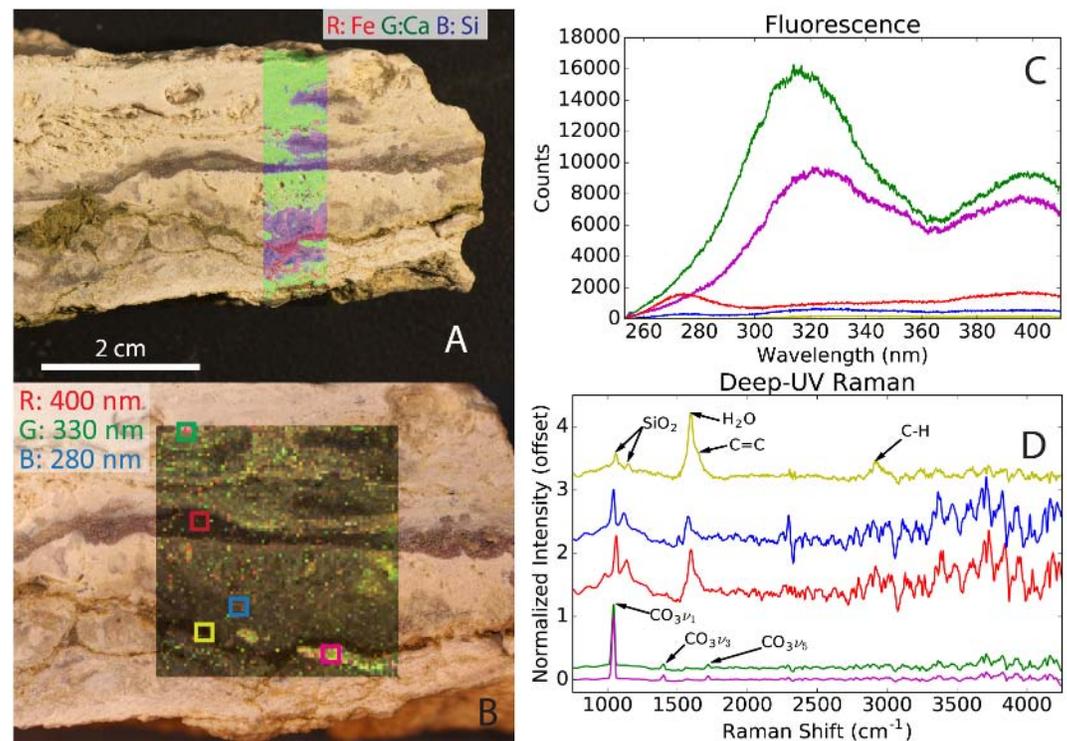
Figure 10. Proximity science results on calcite-bearing sample CR025 (carbonate-rich unit ML) with bands of chalcedony and an Fe-bearing silicate. (a) PIXL-like image with overlay of elemental abundance for CR025. (b) Low-resolution fluorescence scan map, with averaged (c) UV fluorescence and (d) Raman spectra from the highlighted areas shown below.

exterior florescence spectra from the same rock typically exhibit similar maxima, suggesting that the fluorescence observed is originating from organics held within the rocks, and not simply from airfall organic contamination common on the Earth. The wavelength of florescence maxima indicates the class of organic molecule observed (Berlman, 1971). The fluorescence spectra of the carbonate (unit ML; Figure 10c) have a peak near 325 nm, suggesting the presence of organic material related to bacterial flora (Figure 11 and Table 6). Some fluorescence peaks appear to correlate with rock type; carbonates tend to have peaks at 310–320 nm and exotic metamorphic clasts from the scree slope have peaks at 260 and 340 nm (Figure 11). Statistically representative sampling was not done on a sample-by-sample basis, so these correlations are purely qualitative. Differing rock types from the other units have more scattered peak wavelengths, varying significantly by sample (Figure 11). The quick scan results guided follow-up targeting with higher resolution, 100 μm spacing and 1,200 laser pulses per point, deep-UV Raman to search for more specific organic signatures.

Single-point SHERLOC deep-UV Raman spectra show peaks due to sulfate and carbonate anions (Figure 12a), as expected given the information from the other data sets. Conversely, the Raman signal from silicate minerals appears to be weak or nonexistent (depending on the mineral) in simulated SHERLOC point spectra. SHERLOC Raman data <800 cm^{-1} are not collected due to a filter designed to avoid Rayleigh scattering from the sample. The major peaks in silicate Raman spectra tend to be <800 cm^{-1}; however, a phyllosilicate-related broad feature at ~1,100 cm^{-1} and a quartz doublet feature at ~1,050 and 1,120 cm^{-1} are apparent in these spectra when averaging ~100 spectra (Figures 9h and 10d; Nakamoto, 2008). Multipoint averaging also revealed a weak OH-related feature in a ground truth-confirmed sample of montmorillonite (Figure 12b).

In deep-UV Raman data, the appearance of a broad, asymmetric peak at 1,600 cm^{-1} is the primary indicator of carbon-rich material (Figures 9h and 10d), which is caused by an in-plane C=C stretching mode of poly-aromatic carbonaceous material (Socrates, 2004). Its broadening may be due to high defect density, which could signify that the material is relatively pristine (i.e., has not been significantly graphitized; Beyssac
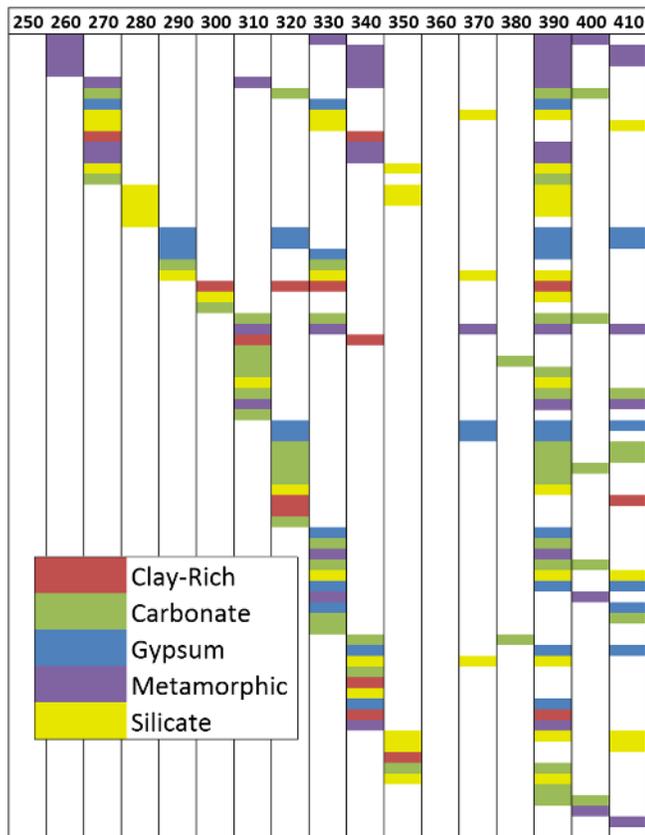
Figure 11. Fluorescence spectral classes observed in targets, classified by the dominant type of material in the sample. Each peak observed in a given spectrum was placed within a 10-nm wavelength bin and targets are classified by type. Spectra in a single sample with the same peak locations are not repeated on the chart. See Table 4 for potential fluorescence spectral classification.

et al., 2004). Low signal-to-noise ratio makes detection of other organic peaks difficult, with one exception: the chalcedony in sample CR025 (unit ML/Mc; Figure 10d) exhibits sufficiently intense signal that an ~2,900-cm^{-1} peak from C–H stretching modes (Socrates, 2004) can clearly be identified. This association between strong Raman signal of unaltered organics and directly precipitated silica deposits would be highly intriguing in a Mars context.

3.3. Sampling Decisions

SHERLOC Raman and fluorescence spectra, along with PIXL data, will allow determination of petrology of a given unit and detection of the organics within the rock. This information is vital in determining whether to take a sample from a specific locality, and, once the decision has been made to sample, which section of the rock to sample from. In the case of this outcrop, at least three samples would likely be considered for caching (not counting duplicates or blanks). The calcite-bearing (ML) unit would be intriguing from a geological perspective immediately upon its detection due to the scarcity of carbonate detections (especially Ca-carbonates) on Mars and their relevance to the climatic history of the planet (Ehlmann & Edwards, 2014; Hu et al., 2015). The determination that the calcite represents a travertine deposit, and especially with the presence of associated silica and organics, makes it a high-priority target for both understanding Martian climate/geological history and seeking biosignatures of past life on Mars. A travertine sample would be important because one of the key factors in biosignature preservation is rapid entrapment, including in fine-grained chemical precipitates (Farmer & Des Marais, 1999). Gypsum has also been noted as a potential preserver of microfossils on Mars (Schopf et al., 2012). On Earth, it is largely disfavored due to its solubility (and consequently rare preservation without recrystallization in ancient deposits), although this is less of a problem in Mars exploration due to the paucity of water after the Hesperian period (Bibring et al., 2006). Finally, low-energy environments with sedimentation of clay-rich mudstones concentrate organics on Earth (Kennedy et al., 2002) and are considered a promising location for preservation of organic molecules on Mars (Summons et al., 2008). Therefore, a sample from the base of the laminated mudstone (LB) unit would likely be considered for potential caching.

4. Discussion

4.1. "Rover" Versus Ground Truth Data Environmental Interpretation

The map composed using data from simulated Mars-2020 remote sensing instruments is largely consistent with the ground truth map of the outcrop, at least from a mineralogical standpoint (Figures 2 and 4). The success of the mineralogical and compositional characterization of the scene primarily with simulated SuperCam data, in combination with the high-resolution simulated color Mastcam-Z and Navcam images, allowed identification of multiple sedimentary deposits, correctly interpreted as primarily lacustrine in origin. Mars-2020 simulated data sets also suggested a lake dominated by subaqueous deposition of clay minerals progressing to a more ephemeral lake system higher in the stratigraphic section, with potential local groundwater/hydrothermal activity resulting in deposition of the carbonate unit. These Mars-2020-like paleoenvironmental interpretations closely match the high-level paleoenvironmental interpretations based on ground truth data and prior literature.

One important aspect of the geology that was not readily recognized from simulated rover remote sensing data is the presence of numerous beds of volcanic ash interbedded with mudstones of purely lacustrine origin. The most likely immediate interpretation of these lighter-toned beds could simply be erosion of alternating source regions, without specific attributions as to the nature of those regions. Even in terrestrial settings,

Table 6
Literature Data on Attributions for Individual Fluorescence Peaks

Fluorescence peak (nm)	Molecular attribution	Reference
280	One-ring aromatics	Bhartia et al. (2008)
290	Bacterial spores	Bhartia et al. (2008)
326	Bacterial vegetative cells	Bhartia et al. (2008)
330	Two-ring aromatics	Bhartia et al. (2008)
350	Indoles	Bhartia et al. (2008)
350	Proteins	Beegle et al. (2015)
364	Bent three-ring aromatics	Bhartia et al. (2008)
374	Linear three-/bent four-ring aromatics	Bhartia et al. (2008)
458	Humic substances	Yamashita et al. (2008)
464	Linear four-/bent five-ring aromatics	Bhartia et al. (2008)

recognition of ash beds can be difficult, especially in cross section, and SEM imaging to reveal highly angular glassy components at a nanoscale is considered diagnostic. The lack of uniquely distinguishing features in ash deposits at a microscale to macroscale in rover remote sensing and proximity data must, therefore, be appreciated and care must be taken to positively identify any such potential deposit. There is no single data set in this study which conclusively could be used to determine the presence of ash in the outcrop. A plausible strategy for consistent recognition of tephras relies on multiple steps of increasing scrutiny to determine a given sedimentary layer's origin: (1) recognition of an abrupt change in color or texture as in the decorrelation stretch shown in Figure 4b, (2) microimaging to probe for a fine and well-sorted grain size and/or accretionary lapilli, and (3) analysis with the spectral and chemical instruments to confirm glassiness, bulk chemical changes (e.g., increases in alkali elements), and/or slight changes in the incompatible element composition of the bed. In this case, ash collection would not calibrate Martian crater-density-based ages (i.e., the exposure is not a surface), but rather establish the absolute timing and deposition rate of sediments at this site. Top surfaces of the underlying sedimentary units would then be bounded by a minimum age, while overlying sediments would be bounded by a maximum age. The ability to derive an absolute age of deposition would be useful for interpretation of the climatic history of Mars and the timing of active lake systems.
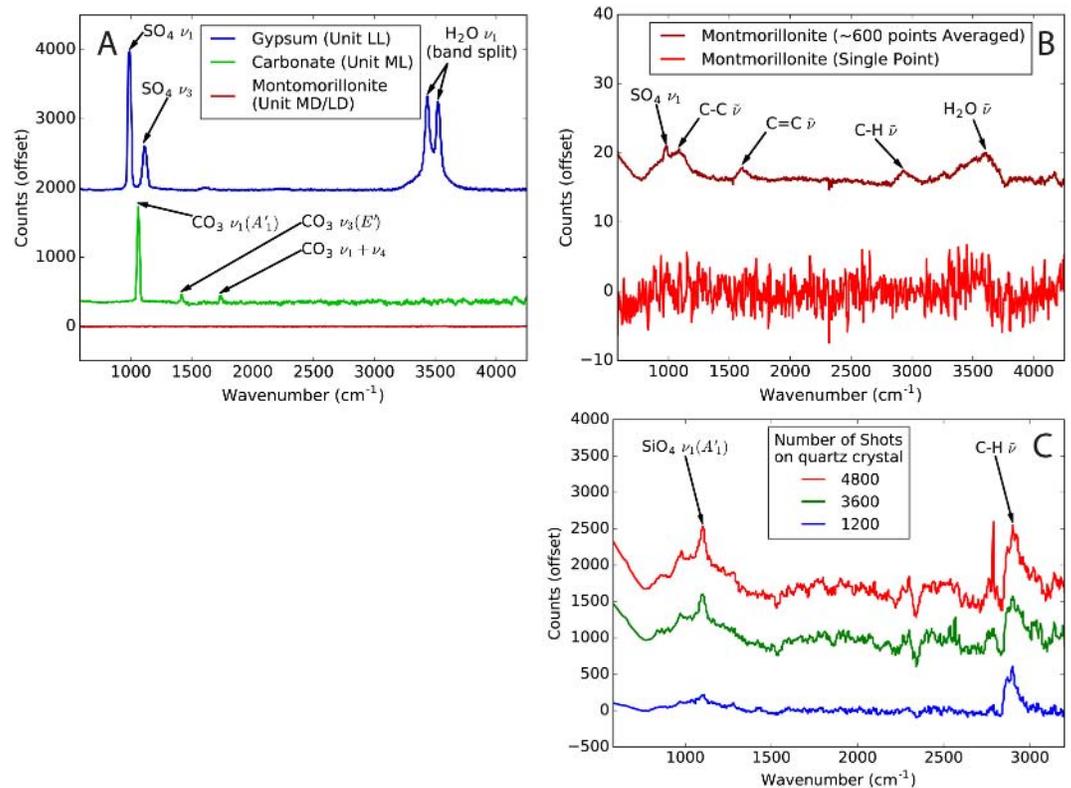
Figure 12. (a) Examples of deep-UV Raman point spectra (samples CR018, CR026, and CR002, listed top to bottom). (b) Spectral features in silicates become more apparent when averaged over a large area (sample CR002), though not with (C, sample CR003) an increase in shot number. (c) Cut off at 3,200 cm^{-1}, beyond which the signal-to-noise ratio falls; the Raman peaks of interest are below this wavenumber. The increasing shot numbers appear to increase fluorescence, which is overwhelming the Raman signal. Inorganic Raman peak designations from Nakamoto (2008).

4.2. Instrument Synergies and Limitations

4.2.1. Mineralogy

All four of the instruments simulated in this study determine mineralogy to varied extents and with different sensitivities. Coarse unit discrimination was possible using Mastcam-Z from a simulated distance of approximately 200 m based on their color, texture, and spectral properties. The distance for initial Mastcam-Z is likely to be smaller than 200 m in practice, lending confidence to the ability of Mastcam-Z to provide effective reconnaissance data. A gypsum-associated 995-nm hydration feature was observed in Mastcam-Z spectra. However, the weak reflectance minimum due to H_2O in phyllosilicates is at 960 nm, where the 1,013 nm filter did not detect it (Figure 6). Thus, on Mars-2020, SuperCam IR point spectra from a distance will be essential for the recognition of hydrated/hydroxylated minerals by features at 1,400 and 1,900 nm and metal OH absorptions from 2,200 to 2,400 nm (Clark et al., 1990). Mineralogy of the mapped units was constrained by analysis of several point spectra from SuperCam.

Calibration of passive spectroscopy (from either Mastcam-Z or SuperCam) may be complicated when performed over a relatively long distance. The longer path length to a given target relative to calibration standards on the rover may introduce uncertainty to the measurement, particularly when atmospheric opacity is high such as during a dust storm. These uncertainties may be somewhat mitigated by performing long-distance spectroscopy close to midday for relatively consistent phase angles.

Iron-related electronic absorptions occur primarily at the wavelengths covered by Mastcam-Z and the SuperCam passive spectral range. This capability will be effective in the context of the more mafic surface mineralogy on Mars. At the outcrop used in this study, variations in iron-related absorptions were in several cases a result of surface weathering rather than being characteristic of the bulk rock. Coverage gaps between 470 and 535 nm and beyond 855 nm in SuperCam's VIS spectra, due to the green Raman laser, may complicate the detection of hematite, which has strong absorptions at ~535 and ~860 nm (Morris et al., 1985). These gaps are covered by the Mastcam-Z filters, meaning that the payload instruments together will acquire the needed information. A more substantive spectral coverage gap occurs between 1,013 and 1,300 nm (Figure 6), which neither Mastcam-Z nor SuperCam has the ability to measure. Pyroxene, olivine, and Fe-bearing feldspars, glasses, and alteration phases have important absorption bands in this wavelength range (Horgan et al., 2014). Variations in pyroxene crystal chemistry, which indicate changing properties of the parent magma, are tracked by examining band shifts between 900 and 1,200 nm (e.g., Klima et al., 2011). Diagnostic band minima will sometimes not be captured in the Mars-2020 data set. To compensate, cross-calibration of passive spectral data in overlapping ranges and synergistic use of SuperCam passive data, the Mastcam-Z longest wavelength channels 975 and 1,013 nm (Bell et al., 2014), and remote elemental composition are likely needed for identifying variations in mafic mineralogy, and PIXL chemistry data or Raman spectroscopy of mineral grains will be used for mafic mineral crystal chemistry as required.

No anticipated vibrational absorptions were missed in the simulated SuperCam IR data set, validating SuperCam's effectiveness in this wavelength range at full resolution and even when spectrally downsampled to ~100 cm^{-1} (Figure 13). The ability to observe VIS and IR absorption features of phyllosilicates, carbonates, sulfates, and iron oxides at a small scale will allow mapping of major alteration mineralogy at a range of distances (see section 4.2.3. below). Due to spectral overlap with CRISM, large-scale mapping may also be confirmed using SuperCam's IR capability, giving the Mars-2020 team the ability to perform strategic route planning based on the confirmation or rejection of CRISM-mapped locations of various mineral deposits with SuperCam passive data. One potential challenge for both Mastcam-Z and SuperCam remote (>7 m distance) observations is the obscuration of target mineralogy by surface dust, which is not simulated in this study. SuperCam can partially avoid this issue within 7 m, as the shock wave from LIBS partially clears the surface. Of course, the DRT can remove dust completely for targets within the arm work zone.

Based on these results, the judicious and frequent selection of SuperCam passive VIS and IR targets using imaging as a guide to delineate the boundaries between suspected lithological/mineralogical units or variations in mineral composition within a distinct unit will be crucial to the effective determination of mineralogy via remote sensing. A potential standard campaign once color Navcam data are acquired could involve (1) full filter set multispectral imaging using Mastcam-Z (downsampled spectrally or spatially if dictated by data volume restrictions, as is common) with SuperCam of each color unit, (2) further SuperCam VIS and IR passive measurements of areas highlighted by Mastcam-Z (perhaps with downsampling for greater time and
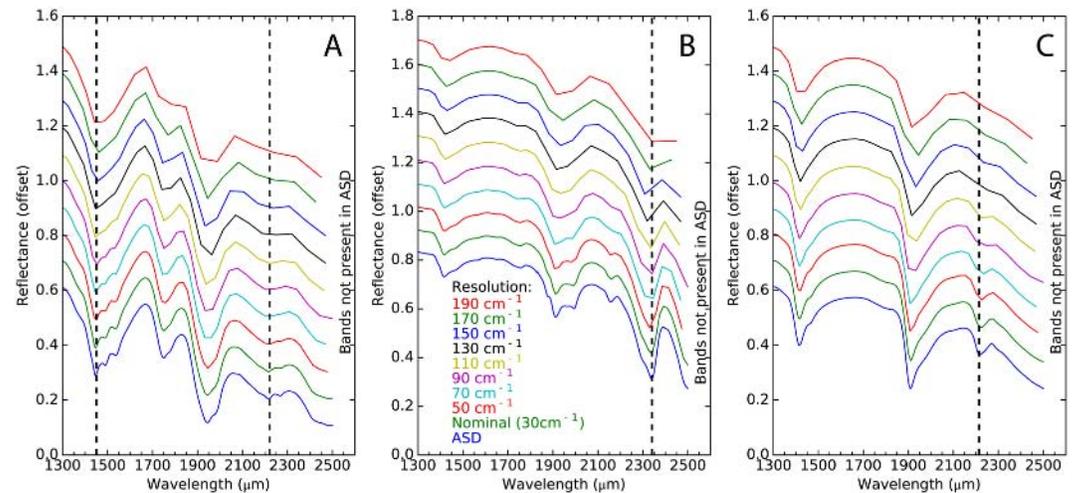
Figure 13. The result of downsampling the resolution of SuperCam passive IR spectra at even spectral sampling to decrease time of acquisition required. It will also be possible to selectively sample portions of the spectrum most diagnostic of minerals of interest. Examples are shown of (a) gypsum-bearing sample CR018 (unit LL), (b) calcite-bearing sample CR026 (unit ML), and (c) montmorillonite-bearing sample CR002 (unit LD).

data volume operational efficiency; see section 4.3), and (3) Mastcam-Z zoom images of areas that potentially exhibit small-scale variability or structure. Follow-up SuperCam spectral transects and Mastcam-Z zoomed full filter set high-resolution images can then be used to elucidate any remaining outstanding ambiguities upon close approach.

The results from the green Raman analog for the SuperCam Raman capability are only partially similar due to the lab instrument's much higher spatial resolution and greater sensitivity compared to SuperCam. However, information about green Raman's relative sensitivities to different minerals is still valuable. The confirmation of minerals detected via passive remote sensing techniques (e.g., gypsum and calcite) and positive identification of quartz (otherwise undetectable to the instruments on Mars-2020) is accomplished with the analog instrument and anticipated for the SuperCam instrument. Montmorillonite was also observed via Raman, although some reference spectra show no major peaks, possibly due to weak Raman scattering cross sections or orientation effects of the grains during generation of the library spectra (Frost & Shurvell, 1997), suggesting that special care should be taken in searching for clay minerals on Mars and in developing appropriate clay reference libraries. The ability to detect minerals with green Raman that cannot be observed by reflectance spectroscopy (and vice versa) make this suite complementary.

SHERLOC detects salt mineral-associated CO_3 (1,050 cm^{-1}), SO_4 (950 and 1,100 cm^{-1}), and H_2O (3,500 cm^{-1}) in single-point spectra collected in milliseconds. The identification of silicates, especially clays, proved more difficult and in our study required the additional collection of hundreds of data points as the dominant SiO_2 Raman feature (~465 cm^{-1}) is cut off by the instrumental notch filter that removes unwanted Rayleigh scattering at Raman shifts <800 cm^{-1}. The relative weakness of spectral features of silicate minerals in the SHERLOC-observable range is likely a result of the smaller interrogation area probed due to the relative opacity of silicates to the UV laser compared with sulfates and carbonates and a lack of resonance effects due to the excitation wavelength of 248.6 nm. By increasing the number of laser shots in a single quartz crystal, the ~1,100 cm^{-1} SiO_4-related feature was observed (Figure 12c). However, at higher wave numbers the signal-to-noise ratio falls due to fluorescence, making this technique less effective in the higher wave number range for these samples. By averaging several individual spectra taken over a small area, hydration features of montmorillonite from unit LD (XRD confirmed to contain abundant smectites; sample CR002 in Table 3) were detected, suggesting multipoint averaging as a potential method of silicate mineral detection by deep-UV Raman if other methods are not available. Quartz was also detected in this way in sample CR025 (Figure 10d), confirming multipoint averaging as a reliable technique for teasing weak (but present) mineral features from the spectra. Given the importance of identifying and interpreting silica and clay minerals to understanding the nature and extent of interactions of water with Martian materials, cross-instrument

strategies for their analysis by other methods (e.g., IR spectroscopy, PIXL crystal chemistry estimates from elemental composition) are necessary and should be incorporated in the routine workflow during outcrop examination.

4.2.2. Chemistry

Major-element abundances determined using LIBS compare favorably with the bulk chemistry measured as part of the ground truth data (see Table 4 and Figure 7). The simple model used provided data with sufficient accuracy for the purposes of this study although, as expected, it resulted in larger uncertainties and deviations from the true chemistry than LIBS is capable of achieving using the more sophisticated submodel approaches available (Anderson et al., 2017). The absolute uncertainties in this analysis were not constrained, but are likely to be $<\pm 5$ wt %; see Anderson et al. (2011) for a detailed discussion of LIBs uncertainties. This simplified model is likely partially responsible for small variations from a one-to-one correlation between LIBS and bulk lithochemistry as is the fact that LIBS has a small spot size, leading to large (real) variations between grain-scale versus bulk lithochemistry data. Very large differences in chemistry between mudstone, tuff, carbonates, and sulfates meant mapping and characterization of the different units could be done on the basis of just a few elements. Although we did not simulate it here, quantification of H, Li, B, F, Cr, Mn, Cl, Ni, Rb, Sr, and Ba will also be possible on Mars-2020 as with Mars Science Laboratory (e.g., Gasda et al., 2017; Lanza et al., 2014; Payré et al., 2017; Rapin et al., 2017; Thomas et al., 2018, 2019). In addition to providing routine chemical analysis, LIBS data from SuperCam will function in a reconnaissance capacity, searching for chemically unusual targets to be more closely investigated by the other instruments in the Mars-2020 suite.

Simulated PIXL demonstrated the ability to observe submillimeter spatial patterns in chemistry (e.g., Figures 9 and 10). This ability will be revealing for the characterization of the geological history of a given rock, the targeting of potential biosignatures for further analysis by SHERLOC, and sampling target downselection. For example, targets high in zirconium such as found here would be prioritized for geochronology, and samples with clear growth texture relationships allowing straightforward interpretation of the time relationships between sample components would be desirable. PIXL's ability to detect trace elements at small spatial scale may give insight to the redox, pH, and weathering history of the rock, which can inform our understanding of the geological and diagenetic history of a rock at that small scale, as well as suggest the presence of potential biosignatures (Mustard et al., 2013). Both SuperCam LIBS and PIXL provided additional evidence to support mineralogy determinations that were made by the other techniques. PIXL's capabilities on Mars-2020 will be greater than simulated here because of the ability to quantify as well as map the spatial distribution of elements. PIXL can also be used both to determine grain-scale chemistry for coarse rocks or sediments and establish the quantitative bulk chemistry of a given target by averaging across a full-sized map.

In the case of analyses of fine-grained rocks such as a mudstone, neither SuperCam LIBS nor PIXL has the spatial resolution to determine the chemistry of individual grains. This challenge of small grain sizes may be solved by statistical unmixing to find mineral/chemical end-members within a given target or group of targets. With both instruments, bulk chemistry can always be observed by multipoint averaging, yielding data similar to APXS measurements familiar from past rover missions (Gellert et al., 2013; Golombek, 1997; Rieder et al., 2003). Additionally, a method has been developed for estimating relative grain size from the compositional spread of the observation points within a ChemCam raster (Rivera-Hernández et al., 2018). At large grain size, individual grains will dominate the chemistry as measured at one point, thus increasing the variability between points, while a grain size much smaller than the laser spot size will yield more consistent chemistry between points (Rivera-Hernández et al., 2018). This technique requires that samples with large grain size exhibit chemical variability and that diagenetic cements do not dominate at large grain size, as cement may cause the sample's chemistry to appear more homogenous than its true bulk chemistry. Presumably PIXL could use this method for individual pixels, with much greater accuracy for small grain sizes.

4.2.3. Organics

The deep-UV fluorescence results simulating SHERLOC data demonstrated that organics were present throughout all collected samples. Raman detection limits are ~10^{-6} w/w for aromatics and ~10^{-4} w/w for aliphatics, and fluorescence is generally several orders of magnitude more sensitive depending on the specific molecule (Beegle et al., 2017), so detection is fully expected given >0.5 wt % total organic carbon (TOC) in

all samples. Different classes of organic molecules have characteristic maxima (Berlman, 1971), and indeed, the samples showed a variety of fluorescence spectra (Figure 11). That the fluorescence peak locations and rock types shown in Figure 11 correlate poorly suggests that either the organic compounds held within the rocks are relatively uniform (and therefore likely sourced from endolithic microbes) or that this technique is not capable of detecting the differing organics present in the strata despite their differing formation environments. Further work characterizing the fluorescence spectra of organic molecules known to have been preserved in rock would clarify this question. Simulated low-resolution quick scans of three samples spatially mapped organics successfully, giving locations for follow-up targeting with deep-UV Raman (Figures 9 and 10). However, using existing published attributions of fluorescence peak positions (summarized in Table 6), we were not able to constrain the types of organics in the samples. Fluorescence spectroscopy of organics in geological samples is a relatively new, underexplored field. As a result, extensive digitized fluorescence libraries like those used for VNIR, VIS, IR, or green Raman spectral analysis simply do not exist. In order to maximize the effectiveness of SHERLOC's fluorescence capabilities, an effort to construct such libraries for high-resolution fluorescence data is warranted prior to the landing of Mars-2020 in order to be able to interpret organics detections.

Prior work indicates that SHERLOC Deep-UV Raman is capable of detection and identification of organic compounds at thresholds of ~0.1–1 wt % (Abbey et al., 2017). Here all samples have >0.5 wt % TOC. Broad peaks at ~1,600 and ~2,900 cm^{-1} indicate the presence of C=C bonds and C–H bonds in the organic compounds contained in several samples (Figures 9h and 10d). An H_2O bend also generates a Raman peak at ~1,600 cm^{-1} in hydrated samples; these overlapping features may be distinguished by width as mineralogical features tend to be sharper. The observation with the best signal-to-noise ratio is in sample CR025, which includes a strong 1,600 cm^{-1} band in a chalcedony matrix (this sample includes quartz SiO_2 Raman bands; Figure 10d; Nakamoto, 2008), demonstrating that samples with a strong biosignature preservation potential are effectively probed by SHERLOC. These 1,600 cm^{-1} signals have a shoulder, suggesting that they may be a mixture of two peaks: one sharp peak (likely H_2O bending) and one broader peak (likely organic). The 2,900 cm^{-1} peak attributed to C–H is observed only in areas of relatively low fluorescence as the increase in noise due to higher amounts of fluorescence obscure this peak (Figure 10d). Intriguingly, the areas highlighted by fluorescence in the quick scans appear to have generally weaker organic Raman peaks, while the areas with less fluorescence often have the strongest organic Raman peaks (Figures 9 and 10). These results suggest that fluorescence and deep-UV Raman may be complementary to one another, although the more limited areal coverage of the deep-UV Raman means care must be taken to investigate all spectral components of a sample, including fluorescence-dark areas to ensure that strong Raman signals are not missed.

Some organic components (especially at 2,900 cm^{-1}) are visible in the green Raman data as well as the deep-UV data (Figures 7f–7i). In both Raman data sets, it is not possible to identify or classify the organics present in detail due to the broadness of the observed peaks, which likely indicate a wide variety of organics with distinctive molecular structures and chemical environments. The lack of a "D" band (at 1,400 cm^{-1}; Socrates, 2004), the relative intensity of the 2,900 cm^{-1} band, and the broadness of the C=C band at 1,600 cm^{-1} in these samples indicates almost no graphitization of these organics, suggesting that they are rich in aliphatics and may be considered "fresh" organics which are entirely thermally immature. The origin of these fresh organics is ambiguous from these data and could result from entombment at the time of deposition or from modern endolithic microorganisms. On Mars, such pristine organic molecules are unlikely to be observed after ~3 Gyr of preservation due to radiolytic decomposition (Pavlov et al., 2012). The intensity of the organic signals observed here appear to be dependent on the mineral matrix as a result of the integrated volume of the minerals probed by the laser, which suggests that the true detection limit of SHERLOC may depend on the mineral substrate. This possibility should be explored further but is beyond the scope of this work.

4.3. Operational Considerations

In this study, traversability and reachability considerations were ignored and the entire outcrop was treated as though it were accessible. Of course, ancillary remote sensing data will be required for reconnaissance of these parameters for actual Mars-2020 operations. This study also assumes that optimal illumination angles can be achieved for imaging and remote spectral observations of the outcrop, which may not be the case for all outcrop exposures.

As with prior rover missions, day-to-day operations of Mars-2020 will be limited by time, power, and data downlink volume available. Another limitation in an operational setting is the overall complexity of a given plan. In practice, this means that the full range of rover instrumentation presented here for most targets is unlikely to be deployed unless particularly interesting results are obtained from that target. However, selection of sample locations and complete documentation of drill samples is of high importance, meaning that the data crucial to the interpretations provided in this study would likely have been collected.

Our analog study points to a few measurement modes that may minimize resource use without compromising scientific requirements. Mastcam-Z will be capable of providing data compression and transmitting only sections of images to limit the overall data transmission necessary for a given measurement. In addition, by using only a subset of Mastcam-Z filters, both time and data will be saved.

SuperCam uses an acousto-optical tunable filter rather than a diffraction grating to generate high-resolution spectra in the IR range, acquiring data of each wave number step independently (Wiens et al., 2017). Downsampling passive reflectance spectra from the optimal oversampled 15 cm^{-1} or the nominal 30 cm^{-1} resolution (Fouchet et al., 2015) can provide time savings without compromising needed data for initial reconnaissance. For example, three spectra downsampled from the nominal resolution to 190 cm^{-1} show that as low as ~100 cm^{-1}, the mineral class is discernable, depending on the exact mineral in question (Figure 13). It will also be possible to selectively sample portions of the spectral range most diagnostic of mineral classes of interest at the nominal resolution, while lowering the spectral sampling at other wavelengths. Because the SuperCam IR passive data are the only Mars-2020 data suited for detection and distinguishing hydrated/hydroxylated mineral-bearing outcrops in the far field, these lower spectral resolution measurement modes may be highly useful for reconnaissance of potential campaign locations while allowing more efficient rover operations. Of course, follow-on high-resolution spectra are required to move from mineral class to identification of specific minerals (e.g., clay versus montmorillonite or carbonate versus calcite). The ability to select a specific wavelength of measurement in the IR range also allows SuperCam to make rudimentary band depth maps at the outcrop scale by rastering across the outcrop with three specific wavelengths selected to give a band depth at each point, again reducing data needs while permitting large-scale reconnaissance.

Similarly, spatial downsampling of SHERLOC and PIXL may be used to acquire "quick-look" or lower data volume reconnaissance data that remote sensing instruments are unable to easily provide, for example, searching for the presence of organics with SHERLOC or an element like zirconium with PIXL. These modes may also be used for selection of targets for higher-resolution analysis by the same instruments in a given workspace, especially for eventual drill target selection, where comprehensive but low-resolution data will ensure that no important potential drill sites are left uninvestigated.

5. Conclusions

Using data simulating the Mars-2020 instrument suite, an outcrop near China Ranch in the Mojave desert was analyzed in a similar fashion to the likely analytical procedures to be followed in the upcoming mission. Overall, we find that the Mars-2020 instruments are well suited and complement each other to provide rapid reconnaissance for selection of samples to cache. Coarse unit discrimination and target selection was made using the simulated Mastcam-Z color filters, and was further aided by full Mastcam-Z multispectral data, enhanced by the use of decorrelation stretches. SuperCam VIS/IR point spectra were critical to identifying unit composition and compositional variability remotely. Carefully selected transects identified montmorillonite, carbonate, and gypsum-montmorillonite mixtures for each of the units delineated using Mastcam-Z. Together, the Mastcam-Z and SuperCam passive VIS/IR and Raman data allowed mapping of the general mineralogy of units present in the outcrop. LIBS gave reconnaissance-level major element chemistry that allowed further identification of targets for proximity science. The proximity science instruments confirmed expected mineralogy based on chemistry from PIXL; PIXL also identified previously unrecognized trace element patterns that would prompt further investigation and sampling for geochronology. Salts were readily identified and mapped with SHERLOC deep UV spectra. Organics were identified in all collected samples with fluorescence data from SHERLOC with more detailed information provided by deep-UV Raman in some cases. Materials from the carbonate, finely laminated clay mudstones, and gypsiferous mudstones with

organics would likely be considered for sampling and caching. Successful collection and caching of these samples would fulfill the Mars-2020 requirements to examine a site for Mars's geologic/climate history, search for signs of life, and collect and cache samples at this site alone. These results indicate that the instrument suite as simulated in this study is capable of exploration, identification of units of interest, and sampling and caching to support the high-level goals of the Mars-2020 mission.

The study further revealed approaches that could improve science return and operational efficiency and thus warrant further development. First, frequent long-distance scans (from tens of meters) using SuperCam's IR passive capability will be important to discriminate compositional changes in outcrops with otherwise similar colors to avoid missing important mineralogical features during the Mars-2020 mission. As an example, coupling remote sensing with proximity data will be essential for identification of potential glassy ash units useful for age dating. Second, cross-calibration of Mastcam-Z and SuperCam passive data will be required to best recognize and map variation in mafic mineralogy (olivine, pyroxenes, and volcanic glasses), which is most distinct near 1,000–1,300 nm where there is a gap in spectral coverage between the instruments. Third, further investigation should be made of deep UV Raman spectra of silicate (especially phyllosilicate) minerals to understand what operational modes are optimal for their detection, and both green and deep UV Raman spectral libraries of phyllosilicates are needed. Fourth, libraries of specific organic compounds with the potential to be encountered on Mars should be measured with high spectral resolution fluorescence and Raman spectroscopies to equip the rover with a centralized, comprehensive spectral library from which to interpret mission data.

References

Abbey, W. J., Bhartia, R., Beegle, L. W., DeFlores, L., Paez, V., Sijapati, K., et al. (2017). Deep UV Raman spectroscopy for planetary exploration: The search for in situ organics. *Icarus*, *290*, 201–214. https://doi.org/10.1016/j.icarus.2017.01.039

Allwood, A. C., Clark, B., Flannery, D., Hurowitz, J., Wade, L., Elam, T., et al. (2015). Texture-specific elemental analysis of rocks and soils with PIXL: The Planetary Instrument for X-ray Lithochemistry on Mars 2020. In 2015 IEEE Aerospace Conference (pp. 1–13). https://doi.org/10.1109/AERO.2015.7119099

Allwood, A. C., Wade, L. A., & Hurowitz, J. A. (2016). PIXL Investigation on the Mars 2020 Rover (Vol. 4138). Presented at the 3rd International Workshop on Instrumentation for Planetary Mission. Retrieved from http://adsabs.harvard.edu/abs/2016LPICo1980.4138A

Anderson, R.B., Finch, N., Clegg, S., Gaff, T., Morris, R. V., & Laura, J. (2017). Python Spectral Analysis Tool (PySAT) For preprocessing, multivariate analysis, and machine learning with point spectra (Vol. 1986). Presented at the 3rd Planetary Data Workshop, Lunar and Planetary Institute.

Anderson, R. B., Morris, R. V., Clegg, S. M., Bell, J. F., Wiens, R. C., Humphries, S. D., et al. (2011). The influence of multivariate analysis methods and target grain size on the accuracy of remote quantitative chemical analysis of rocks using laser induced breakdown spectroscopy. *Icarus*, *215*(2), 608–627. https://doi.org/10.1016/j.icarus.2011.07.034

Arvidson, R. E., Bell, J. F., Bellutta, P., Cabrol, N. A., Catalano, J. G., Cohen, J., et al. (2010). Spirit Mars Rover Mission: Overview and selected results from the northern Home Plate Winter Haven to the side of Scamander crater. *Journal of Geophysical Research: Planets*, *115*(E7), E00F03. https://doi.org/10.1029/2010JE003633

Beegle, L., Bhartia, R., White, M., DeFlores, L., Abbey, W., Wu, Y.-H., et al. (2015). SHERLOC: Scanning Habitable Environments with Raman and Luminescence for Organics and Chemicals. In *2015 IEEE Aerospace Conference* (pp. 1–11). https://doi.org/10.1109/AERO.2015.7119105

Beegle, L. W., Bhartia, R., Carrier, B., DeFlores, L., Abbey, W., Asher, S., et al. (2017). The SHERLOC investigation (Vol. 48, p. 2839). Presented at the Lunar and Planetary Science Conference. Retrieved from http://adsabs.harvard.edu/abs/2017LPI....48.2839B

Beegle, L. W., Bhartia, R., DeFlores, L., Miller, E., Pollack, R., Abbey, W., & Carrier, B. (2016). SHERLOC: On the road to Mars (Vol. 4117). Presented at the 3rd International Workshop on Instrumentation for Planetary Mission. Retrieved from http://adsabs.harvard.edu/abs/2016LPICo1980.4117B

Bell, J. F., Maki, J. N., Mehall, G. L., Ravine, M. A., & Caplinger, M. A. (2014). *Mastcam-Z: A geologic, stereoscopic, and multispectral investigation on the NASA Mars-2020 rover*. (p. 1151) Greenbelt, Maryland: Presented at the 2nd International Workshop on Instrumentation for Planetary Missions.

Bell, J. F., Maki, J. N., Mehall, G. L., Ravine, M. A., Caplinger, M. A., & Mastcam-Z Team (2016). *Mastcam-Z: Designing a geologic, stereoscopic, and multispectral pair of zoom cameras for the NASA Mars 2020 rover* (Vol. 1980, p. 4126). Pasadena, California: Presented at the 3rd International Workshop on Instrumentation for Planetary Mission. Retrieved from. http://adsabs.harvard.edu/abs/2016LPICo1980.4126B

Bell, J. F., Squyres, S. W., Herkenhoff, K. E., Maki, J. N., Arneson, H. M., Brown, D., et al. (2003). Mars Exploration Rover Athena Panoramic Camera (Pancam) investigation. *Journal of Geophysical Research: Planets*, *108*(E12). https://doi.org/10.1029/2003JE002070

Berlman, I. B. (1971). *Handbook of fluorescence spectra of aromatic compounds*, (p. 342). New York: Acad. Press.

Beyssac, O., Bollinger, L., Avouac, J.-P., & Goffé, B. (2004). Thermal metamorphism in the lesser Himalaya of Nepal determined from Raman spectroscopy of carbonaceous material. *Earth and Planetary Science Letters*, *225*(1), 233–241. https://doi.org/10.1016/j.epsl.2004.05.023

Bhartia, R., Hug, W. F., Salas, E. C., Reid, R. D., Sijapati, K. K., Tsapin, A., Abbey, W., Nealson, K. H, Lane, A. L., & Conrad, P. G. (2008). Classification of Organic and Biological Materials with Deep Ultraviolet Excitation. *Applied Spectroscopy*, *62*(10), 1070–1077.

Bibring, J.-P., Langevin, Y., Mustard, J. F., Poulet, F., Arvidson, R., Gendrin, A., et al. (2006). Global mineralogical and aqueous Mars history derived from OMEGA/Mars Express data. *Science*, *312*(5772), 400–404. https://doi.org/10.1126/science.1122659

Buz, J., Ehlmann, B. L., Kinch, K., Madsen, M. B., Johnson, J. R., Rice, M. S., et al. (2019). Photometric characterization of Lucideon and Avian Technologies color standards including application for calibration of the Mastcam-Z instrument on the Mars 2020 rover. *Optical Engineering*, *58*(02), 027108. https://doi.org/10.1117/1.OE.58.2.027108

Clark, R. N., King, T. V. V., Klejwa, M., Swayze, G. A., & Vergo, N. (1990). High spectral resolution reflectance spectroscopy of minerals. *Journal of Geophysical Research: Solid Earth*, *95*(B8), 12653–12680. https://doi.org/10.1029/JB095iB08p12653

Clegg, S. M., Wiens, R. C., Anderson, R., Forni, O., Frydenvang, J., Lasue, J., et al. (2017). Recalibration of the Mars Science Laboratory ChemCam instrument with an expanded geochemical database. *Spectrochimica Acta Part B: Atomic Spectroscopy*, *129*, 64–85. https://doi.org/10.1016/j.sab.2016.12.003

Edgett, K. S., Ravine, M. A., Caplinger, M. A., Ghaemi, F. T., Schaffner, J. A., Malin, M. C., et al. (2009). *The Mars Science Laboratory (MSL) Mars Hand Lens Imager (MAHLI) Flight Instrument*, (Vol. 40, p. 1197). Woodlands, Texas: Presented at the Lunar and Planetary Science Conference. Retrieved from. http://adsabs.harvard.edu/abs/2009LPI....40.1197E

Ehlmann, B. L., & Edwards, C. S. (2014). Mineralogy of the Martian surface. *Annual Review of Earth and Planetary Sciences*, *42*(1), 291–315. https://doi.org/10.1146/annurev-earth-060313-055024

Ehlmann, B. L., Mustard, J. F., Murchie, S. L., Poulet, F., Bishop, J. L., Brown, A. J., et al. (2008). Orbital identification of carbonate-bearing rocks on Mars. *Science*, *322*(5909), 1828–1832. https://doi.org/10.1126/science.1164759

Farley, K. A. (2017). *Mars 2020 Mission*. Monrovia, California: Presented at the Mars Exploration Program Analysis Group Meeting.

Farmer, J. D., & Des Marais, D. J. (1999). Exploring for a record of ancient Martian life. *Journal of Geophysical Research: Planets*, *104*(E11), 26,977–26,995. https://doi.org/10.1029/1998JE000540

Farrand, W. H., Bell, J. F., Johnson, J. R., Squyres, S. W., Soderblom, J., & Ming, D. W. (2006). Spectral variability among rocks in visible and near-infrared multispectral Pancam data collected at Gusev crater: Examinations using spectral mixture analysis and related techniques. *Journal of Geophysical Research: Planets*, *111*(E2), E02S15. https://doi.org/10.1029/2005JE002495

Fassett, C. I., & Head, J. W. (2005). Fluvial sedimentary deposits on Mars: Ancient deltas in a crater lake in the Nili Fossae region. *Geophysical Research Letters*, *32*(14), L14201. https://doi.org/10.1029/2005GL023456

Fouchet, T., Montmessin, F., Forni, O., Maurice, S., Wiens, R. C., Jonhson, J. R., et al. (2015). The infrared investigation on the SuperCam instrument for the Mars2020 rover (Vol. *46*, p. 1736). Presented at the Lunar and Planetary Science Conference. Retrieved from http://adsabs.harvard.edu/abs/2015LPI....46.1736F

Frost, R. L., & Shurvell, H. F. (1997). Raman microprobe spectroscopy of halloysite. *Clays and Clay Minerals*, *45*(1), 68–72.

Gandin, A., & Capezzuoli, E. (2014). Travertine: Distinctive depositional fabrics of carbonates from thermal spring systems. *Sedimentology*, *61*(1), 264–290. https://doi.org/10.1111/sed.12087

Gasda, P. J., Haldeman, E. B., Wiens, R. C., Rapin, W., Bristow, T. F., Bridges, J. C., et al. (2017). In situ detection of boron by ChemCam on Mars. *Geophysical Research Letters*, *44*(17), 8739–8748. https://doi.org/10.1002/2017GL074480

Gasnault, O., Maurice, S., Wiens, R. C., Le Mouélic, S., Fischer, W. W., Caïs, P., et al. (2015). SuperCam remote micro-imager on Mars 2020 (Vol. *46*, p. 2990). Presented at the Lunar and Planetary Science Conference. Retrieved from http://adsabs.harvard.edu/abs/2015LPI....46.2990G

Gellert, R., Berger, J. A., Boyd, N., Brunet, C., Campbell, J. L., Curry, M., et al. (2013). Initial MSL APXS activities and observations at Gale crater, Mars (Vol. *44*, p. 1432). Presented at the Lunar and Planetary Science Conference. Retrieved from http://adsabs.harvard.edu/abs/2013LPI....44.1432G

Golombek, M. P. (1997). The Mars Pathfinder mission. *Journal of Geophysical Research: Planets*, *102*(E2), 3953–3965. https://doi.org/10.1029/96JE02805

Goudge, T. A., Mustard, J. F., Head, J. W., Fassett, C. I., & Wiseman, S. M. (2015). Assessing the mineralogy of the watershed and fan deposits of the Jezero crater paleolake system, Mars. *Journal of Geophysical Research: Planets*, *120*(4), 2014JE004782. https://doi.org/10.1002/2014JE004782, 775, 808

Grove, C. I. H. (1992). Laboratory reflectance spectra of 160 minerals, 0.4 to 2.5 micrometers. Retrieved from https://ntrs.nasa.gov/search.jsp?R=20070030855

Hillhouse, J. W. (1987). *Late Tertiary and Quaternary geology of the Tecopa Basin, southeastern California (No. USGS/MAP/I-1728)*. Reston, VA (United States): Geological Survey. https://doi.org/10.2172/60181

Hillier, S. (2016). Accurate quantitative analysis of clay and other minerals in sandstones by XRD: Comparison of a Rietveld and a reference intensity ratio (RIR) method and the importance of sample preparation. *Clay Minerals*, *35*(1), 291–302. https://doi.org/10.1180/000985500546666

Horgan, B. H. N., Cloutis, E. A., Mann, P., & Bell, J. F. (2014). Near-infrared spectra of ferrous mineral mixtures and methods for their identification in planetary surface spectra. *Icarus*, *234*, 132–154. https://doi.org/10.1016/j.icarus.2014.02.031

Hu, R., Kass, D. M., Ehlmann, B. L., & Yung, Y. L. (2015). Tracing the fate of carbon and the atmospheric evolution of Mars. *Nature Communications*, *6*(1), 1–9. https://doi.org/10.1038/ncomms10003

Hunt, G. R., & Salisbury, J. W. (1971). Visible and near infrared spectra of minerals and rocks. II. Carbonates. *Modern Geology*, *2*, 23–30.

Hunt, G. R., Salisbury, J. W., & Lenhoff, C. J. (1971). Visible and near infrared spectra of minerals and rocks. IV. Sulphides and sulphates. *Modern Geology*, *3*, 1–14.

Jennings, C. W., Burnett, J. L., & Troxel, B. W. (1962). *Geologic map of California: Trona sheet*. Sacramento, CA: Geologic, California Division of Mines and Geology.

Johnson, J. R., Ruff, S. W., Moersch, J., Roush, T., Horton, K., Bishop, J., et al. (2001). Geological characterization of remote field sites using visible and infrared spectroscopy: Results from the 1999 Marsokhod field test. *Journal of Geophysical Research: Planets*, 7683–7711. https://doi.org/10.1029/1999JE001149@10.1002/(ISSN)2169-9100.MARSOK1, *106*, E4

Kennedy, M. J., Pevear, D. R., & Hill, R. J. (2002). Mineral surface control of organic carbon in black shale. *Science*, *295*(5555), 657–660. https://doi.org/10.1126/science.1066611

Klima, R. L., Dyar, D. M., & Pieters, C. M. (2011). Near-infrared spectra of clinopyroxenes: Effects of calcium content and crystal structure. *Meteoritics & Planetary Science*, *46*(3), 379–395. https://doi.org/10.1111/j.1945-5100.2010.01158.x

Lanza, N. L., Fischer, W. W., Wiens, R. C., Grotzinger, J., Ollila, A. M., Cousin, A., et al. (2014). High manganese concentrations in rocks at Gale crater, Mars. *Geophysical Research Letters*, *41*(16), 5755–5763. https://doi.org/10.1002/2014GL060329

Maki, J. N., McKinney, C. M., Sellar, R. G., Copley-Woods, D. S., Gruel, D. C., Nuding, D. L., et al. (2016). *Enhanced Engineering Cameras (EECAMs) for the Mars 2020 rover* (Vol. 1980, p. 4132). Pasadena, California: Presented at the 3rd International Workshop on Instrumentation for Planetary Mission. Retrieved from http://adsabs.harvard.edu/abs/2016LPICo1980.4132M

Malin, M. C., Ravine, M. A., Caplinger, M. A., Ghaemi, F. T., Schaffner, J. A., Maki, J. N., et al. (2017). The Mars Science Laboratory (MSL) Mast cameras and Descent imager: Investigation and instrument descriptions. *Earth and Space Science*, *4*(8), 506–539. https://doi.org/10.1002/2016EA000252

Mason, J. F. (1948). Geology of the Tecopa Area, southeastern California. *GSA Bulletin*, *59*(4), 333–352. https://doi.org/10.1130/0016-7606 (1948)59[333:GOTTAS]2.0.CO;2

Maurice, S., Wiens, R. C., Saccoccio, M., Barraclough, B., Gasnault, O., Forni, O., et al. (2012). The ChemCam instrument suite on the Mars Science Laboratory (MSL) rover: Science objectives and mast unit description. *Space Science Reviews*, *170*(1-4), 95–166. https://doi.org/10.1007/s11214-012-9912-2

Morris, R. V., Lauer, H. V., Lawson, C. A., Gibson, E. K., Nace, G. A., & Stewart, C. (1985). Spectral and other physicochemical properties of submicron powders of hematite (α-Fe_2O_3), maghemite (γ-Fe_2O_3), magnetite (Fe_3O_4), goethite (α-FeOOH), and lepidocrocite (γ-FeOOH). *Journal of Geophysical Research: Solid Earth*, *90*(B4), 3126–3144. https://doi.org/10.1029/JB090iB04p03126

Mustard, J. F., Adler, M., Allwood, A. C., Bass, D. S., Beaty, D. W., Bell, J. F., et al. (2013). Report of the Mars 2020 Science Definition Team. *Mars Exploration Program Analysis Group*, *154*.

Nakamoto, K. (2008). *Infrared and Raman spectra of inorganic and coordination compounds, Part A: Theory and applications in inorganic chemistry*. John Wiley & Sons.

Pavlov, A. A., Vasilyev, G., Ostryakov, V. M., Pavlov, A. K., & Mahaffy, P. (2012). Degradation of the organic molecules in the shallow subsurface of Mars due to irradiation by cosmic rays. *Geophysical Research Letters*, *39*(13), n/a. https://doi.org/10.1029/2012GL052166

Payré, V., Fabre, C., Cousin, A., Sautter, V., Wiens, R. C., Forni, O., et al. (2017). Alkali trace elements in Gale crater, Mars, with ChemCam: Calibration update and geological implications. *Journal of Geophysical Research: Planets*, *122*(3), 650–679. https://doi.org/10.1002/2016JE005201

Rapin, W., Meslin, P.-Y., Maurice, S., Wiens, R. C., Laporte, D., Chauviré, B., et al. (2017). Quantification of water content by laser induced breakdown spectroscopy on Mars. *Spectrochimica Acta Part B: Atomic Spectroscopy*, *130*, 82–100. https://doi.org/10.1016/j.sab.2017.02.007

Rice, M. S., Bell, J. F., Cloutis, E. A., Wang, A., Ruff, S. W., Craig, M. A., et al. (2010). Silica-rich deposits and hydrated minerals at Gusev crater, Mars: Vis-NIR spectral characterization and regional mapping. *Icarus*, *205*(2), 375–395. https://doi.org/10.1016/j.icarus.2009.03.035

Rieder, R., Gellert, R., Brückner, J., Klingelhöfer, G., Dreibus, G., Yen, A., & Squyres, S. W. (2003). The new Athena alpha particle X-ray spectrometer for the Mars Exploration Rovers. *Journal of Geophysical Research: Planets*, *108*(E12), 8066. https://doi.org/10.1029/2003JE002150

Rivera-Hernández, F., Sumner, D. Y., Mangold, N., Stack, K. M., Forni, O., Newsom, H., et al. (2018). *Using ChemCam LIBS data to constrain grain size in rocks on*. Mars: Proof of concept and application to rocks at Yellowknife Bay and Pahrump Hills, Gale crater. *Icarus*. https://doi.org/10.1016/j.icarus.2018.10.023

Schofield, R. E., Hurowitz, J. A., Parise, J. B., Zhong, H., Allwood, A., Flannery, D., & Hodyss, R. (2017). Using diffraction peaks in X-ray fluorescence spectra from the Mars 2020 PIXL instrument for mineral phase identification (vol. 48, p. 2955). Presented at the Lunar and Planetary Science Conference. Retrieved from http://adsabs.harvard.edu/abs/2017LPI....48.2955S

Schopf, J. W., Farmer, J. D., Foster, I. S., Kudryavtsev, A. B., Gallardo, V. A., & Espinoza, C. (2012). Gypsum-permineralized microfossils and their relevance to the search for life on Mars. *Astrobiology*, *12*(7), 619–633. https://doi.org/10.1089/ast.2012.0827

Smith, P. H., Tomasko, M. G., Britt, D., Crowe, D. G., Reid, R., Keller, H. U., et al. (1997). The imager for Mars Pathfinder experiment. *Journal of Geophysical Research: Planets*, *102*(E2), 4003–4025. https://doi.org/10.1029/96JE03568

Socrates, G. (2004). *Infrared and Raman characteristic group frequencies: Tables and charts*. Hoboken, New Jersey: John Wiley & Sons.

Summons, R. E., Albrecht, P., McDonald, G., & Moldowan, J. M. (2008). Molecular biosignatures. *Space Science Reviews*, *135*(1–4), 133–159. https://doi.org/10.1007/s11214-007-9256-5

Thomas, N. H., Ehlmann, B. L., Anderson, D. E., Clegg, S. M., Forni, O., Schröder, S., et al. (2018). Characterization of hydrogen in basaltic materials with laser-induced breakdown spectroscopy (LIBS) for application to MSL ChemCam data. *Journal of Geophysical Research: Planets*, In Press, *123*(8), 1996–2021. https://doi.org/10.1029/2017JE005467

Thomas, N. H., Ehlmann, B. L., Meslin, P.-Y., Rapin, W., Anderson, D. E., Rivera-Hernández, F., et al. (2019). Mars Science Laboratory observations of chloride salts in Gale crater, Mars. *Geophysical Research Letters*, *46*(19), 10,754–10,763. https://doi.org/10.1029/2019GL082764

Van Gorp, B., Mouroulis, P., Blaney, D., Green, R. O., Ehlmann, B. L., & Rodriguez, J. I. (2014). Ultra-compact imaging spectrometer for remote, in situ, and microscopic planetary mineralogy. *Journal of Applied Remote Sensing*, *8*(1), Art. No. 084988.

Wang, A., Freeman, J. J., & Jolliff, B. L. (2015). Understanding the Raman spectral features of phyllosilicates. *Journal of Raman Spectroscopy*, *46*(10), 829–845. https://doi.org/10.1002/jrs.4680

Wiens, R. C., Maurice, S., & Perez, F. R. (2017). The SuperCam remote sensing instrument suite for the Mars 2020 rover: A preview. *Spectroscopy Online*, *32*(5), 50–55.

Wiens, R. C., Maurice, S., Barraclough, B., Saccoccio, M., Barkley, W. C., Bell, J. F., et al. (2012). The ChemCam instrument suite on the Mars Science Laboratory (MSL) rover: Body unit and combined system tests. *Space Science Reviews*, *170*(1-4), 167–227. https://doi.org/10.1007/s11214-012-9902-4

Williford, K. H., Farley, K. A., Stack, K. M., Allwood, A. C., Beaty, D., Beegle, L. W., et al. (2018). Chapter 11: The NASA Mars 2020 rover mission and the search for extraterrestrial life. In N. A. Cabrol, & E. A. Grin (Eds.), *From Habitability to Life on Mars* (pp. 275–308). Amsterdam, Netherlands: Elsevier. https://doi.org/10.1016/B978-0-12-809935-3.00010-4

Yamashita, Y., Jaffé, R., Maie, N., & Tanoue, E. (2008). Assessing the dynamics of dissolved organic matter (DOM) in coastal environments by excitation emission matrix fluorescence and parallel factor analysis (EEM-PARAFAC). *Limnology and Oceanography*, *53*(5), 1900–1908. https://doi.org/10.4319/lo.2008.53.5.1900